Universiteit Utrecht

IMAU
Institute for Marine and Atmospheric research Utrecht

Faculty of Science

Isentropic meridional mass transport by baroclinic waves and the annular mode

Master thesis

B.A.J. Ammerlaan

Study: Meteorology, Physical Oceanography and Climate

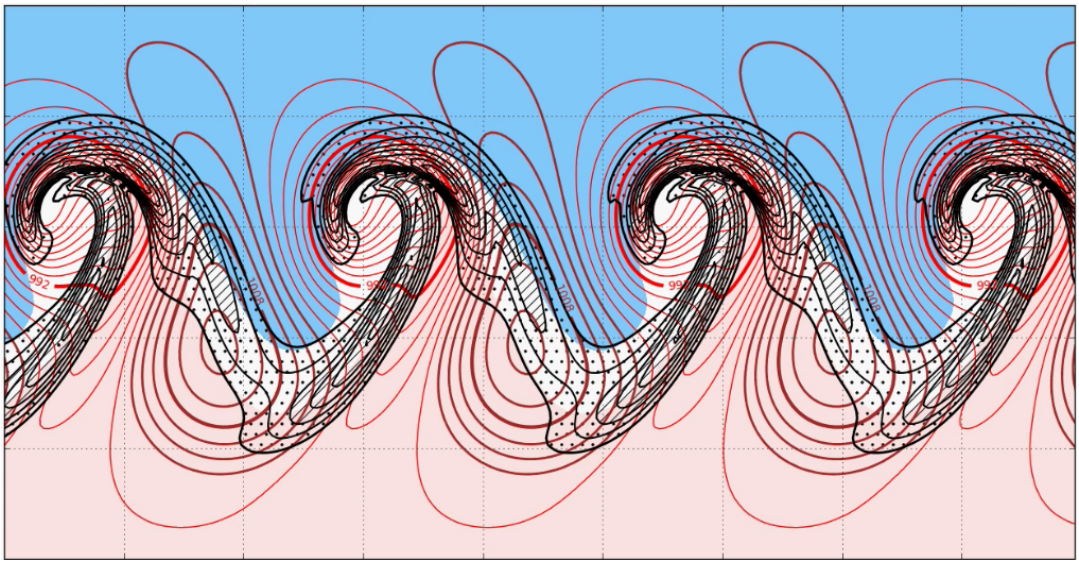

Supervisor:

Dr. A.J. van Delden
Institute of Marine and Atmospheric Research Utrecht

Version June 2018

ABSTRACT

Baroclinic life cycles[1] are simulated by a 25 layer primitive equation model with the aim to investigate the isentropic meridional mass flux (MMF). The development of perturbed fronts with its associated jet is studied for different model parameters and initial conditions. For equal model parameters, the developing situation differs for a different initial wave number on the perturbed front. Wave number 5 develops a wave train with no growth and decay, whereas wave number 6 sustains growing and decaying baroclinic life cycles. The different solutions can be compared to different phases of the Northern Annular Mode (NAM) index in the real atmosphere by looking at the isentropic meridional mass fluxes (MMF) and isentropic meridional potential vorticity substance fluxes (MPF). A perfect translation of the NAM is not found in the model. However, the different solutions of the model have some similarities with the positive or negative NAM phase.

An increase in the Newtonian cooling coefficient, a parametrisation of radiation, and an decrease in the static stability both lead to stronger northward MMF in the midlatitudinal upper troposphere. An increase in the strength of the jet leads to an increased MMF. A wider and weaker initial jet leads to a smaller MMF than a smaller and stronger initial jet.

A specific region with a higher Newtonian cooling coefficient leads to the formation of baroclinic life cycles downstream of the region. Even with a Newtonian cooling coefficient equal to zero and an initial zonal jet, baroclinic waves can grow due to downstream development.

[1] Figure on front page: a snap shot of a model run. In the figure, a typical growth stage of a baroclinic life cycle is visible. The temperature and temperature gradient are shown on the 850 hPa level. The surface pressure is also plotted.

CONTENTS

1. INTRODUCTION

1.1 General circulation of the atmosphere

The Sun does not radiate the same amount of energy to every location on Earth. The differential heating of the surface leads to a higher equilibrium temperature of the surface at the equator than at the poles. The atmosphere is attempting to reduce this temperature difference. Hadley (1735) was the first to notice that the imbalance in insolation induces a direct circulation to transport heat towards the poles. He argued that warm air at the equator rises, because it has a lower density than the cooler air in the surrounding regions. Higher in the atmosphere, the air flows away to the north and south and cools down. Above the polar regions, the air becomes denser by radiative cooling, causing the air to sinks down to the surface where it returns back to the equator.

Furthermore, the air does not follow the meridians, but is deflected to the west at the equator and to the east at the midlatitudes. The rotation of the Earth causes the deflection the currents to the right in the northern hemisphere and to the left in the southern hemisphere, which is known as the Coriolis effect (Lorenz, 1967).

Observations show that the midlatitude westerlies at the Earth's surface have a prevailing direction from south to north and not, as Hadley proposed, from north to south (Ferrel, 1859; Thomson, 1892). An indirect frictionally induced cell at the midlatitudes was added in the theory of the general circulation to account for these observations. The indirect cell was shallow and was assumed to circulate below the cell proposed by Hadley.

Later, it was acknowledged that the Hadley circulation cannot reach further than 25° to 30° (Held and Hou, 1980; Schneider, 2006). The angular momentum per unit mass of a zonal ring of air is given by $M = (\Omega a \cos\phi + [u])a\cos\phi$, where Ω is the angular speed of the Earth, a is the radius of the Earth, $[u]$ is the zonal mean velocity and ϕ is the latitude. If the zonal mean velocity of air at the equator is 0, the conservation of angular momentum implies a zonal mean velocity of $[u] = 91$ m s^{-1} at 25°, which is higher than observed. The angular momentum thus cannot be conserved and a drag force is needed to slow down the flow. Held and Hou (1980) formulated a two layer model of the Hadley circulation. The lower layer is a motionless layer on top of which a layer with a constant zonal velocity is positioned. In the top layer, the angular momentum is conserved. Simultaneously, the model maintains thermal wind balance with the meridional temperature gradient. The zonal mean thermal wind balance is given by (Holton and Hakim, 2012; van Delden, 2017)

$$2\Omega \sin\phi \frac{\partial [u]}{\partial z} = -\frac{g}{\theta_0}\frac{\partial [\theta]}{\partial y} \tag{1.1}$$

where y is the meridional coordinate, z is the vertical coordinate, g is the gravitational acceleration, θ_0 is the reference potential temperature, and $[\theta]$ is the zonal mean potential temperature. With their model, Held and Hou estimated the correct extent of the Hadley circulation.

With the Hadley circulation only reaching the subtropics, the zonal mean general circulation can be split into three major cells: the Hadley cell, the Ferrel cell and the polar cell. However, the Ferrel cell is not thermally driven and should have a different mechanism than the other two cells. In fact, the Ferrel cell is a result of zonally averaging the velocity field. At midlatitudes, heat is still transported poleward. Most of the transport at midlatitudes is caused by zonal asymmetries, which are called eddies.

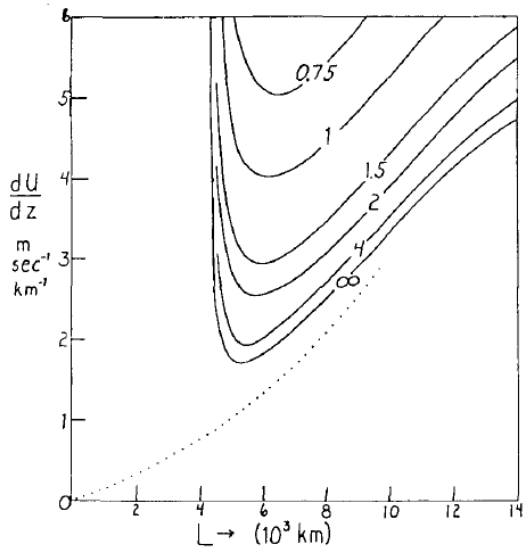

Fig. 1.1: The time in days required for an unstable wave in the two-level model to double its amplitude, given as a function of the vertical wind shear in the basic current and the wavelength. The dotted line represents the curve $v_i = 0$ for the perturbation analyses of Charney (1947) and Kuo (1952). Figure and caption taken from Phillips (1954).

1.2 Baroclinic life cycles and storm tracks

In the midlatitudes, large scale eddies are formed by the process of baroclinic instability (Blackmon, 1976; Lau and Wallace, 1979). Baroclinic instability is associated with a slope difference between isobaric and isentropic planes (Holton and Hakim, 2012; van Delden, 2017). The latitudinal confined region in which most of the baroclinic instabilities develop, is referred to as storm tracks (Hoskins and Valdes, 1990). Diabatic processes cause baroclinically unstable regions. The life cycle of a baroclinic eddy can be simulated in a simplified model and was done by various groups (e.g. Phillips (1956); Simmons and Hoskins (1978); Chang and Orlanski (1993); Thorncroft et al. (1993); van Delden (2017)).

The highest baroclinicity, a measure for how baroclinically unstable the atmosphere is, is often measured by the Eady growth rate (Lindzen and Farrell, 1980)

$$\sigma_{\mathrm{BI}} = 0.31 \frac{f}{N} \left| \frac{\partial \mathbf{v}}{\partial z} \right| \tag{1.2}$$

where $f = 2\Omega \sin\phi$ is the Coriolis parameter, N is the static stability and $\mathbf{v}$ is the horizontal velocity. The highest baroclinicity is found in the western parts of the Pacific and Atlantic basin (Hoskins and Valdes, 1990; Novak et al., 2015). The corresponding strong temperature gradient will be reduced by the formation of a depression, which transports heat northward. Diabatic heating recovers the baroclinic instablity again and the cycle then repeats (Novak et al., 2017).

By perturbation analysis, the instability of a baroclinic wave can be calculated. Phillips (1954) calculated the time required for a baroclinic wave to double in amplitude in a two layer model. The result of his calculation is given in Figure 1.1, where we see that an increasing shear leads to a higher growth rate. Furthermore, the wave length of the baroclinic wave is important for the growth rate. Too short waves are always stable and too long waves need excessive shear values to be unstable.

A more thorough perturbation analysis results in a dispersion relation for baroclinic Rossby waves. In the context of a two layer model and assuming only waves in x-direction, the dispersion

relation is given by (van Delden, 2017)

$$\omega(k) = kU_M - \frac{\beta\left(k^2+\lambda^2\right)}{k\left(k^2+2\lambda^2\right)} \pm \sqrt{\delta} \tag{1.3}$$

where U_M is the mean zonal wind speed, k is the total wave number, λ is a parameter that is related to the inverse of the Rossby deformation radius and in a two layer model given by

$$\lambda^2 \equiv \frac{f_0^2}{\sigma(\delta p)^2} \tag{1.4}$$

where δp is the difference in pressure between the two model levels and σ is the static stability, given by

$$\sigma = -\frac{RT_0}{p}\frac{d\ln\theta_0}{dp} \tag{1.5}$$

where R is the gas constant and T_0 is the reference temperature. The parameter δ in Equation 1.3 is given by

$$\delta = \frac{\beta^2\lambda^4}{k^2\left(k^2+2\lambda^2\right)^2} - \frac{U_T^2k^2\left(2\lambda^2-k^2\right)}{\left(k^2+2\lambda^2\right)} \tag{1.6}$$

where U_T is the velocity difference between the two model levels. From the dispersion relation, we can calculate the phase and group speed of the Rossby wave. If $U_T = 0$, the wave is called a barotropic Rossby wave and the group and phase speed are given by relatively simple relations. In a baroclinic life cycle, we expect however baroclinic Rossby waves, which have more complicated relations for the phase and group speed. In this regime, a special case exits where the phase speed equals the group speed. The criterion for this so called dispersionless case is

$$U_T = \pm\frac{\beta}{2\lambda^2} \tag{1.7}$$

which implies that the difference of the zonal mean zonal velocity between 250 hPa and 750 hPa should be around 5 m s^{-1} in our model runs.

Chang and Orlanski (1993) showed that the largest eddy activity is not necessarily in the regions with highest baroclinicity. In the western ocean basins, baroclinic instability is highest. Because the group speed is often higher than the phase speed, the eddy energy radiates from regions with high baroclinicity to regions with a lower baroclinicity, where eddy activity peaks. Further downstream, the eddies dissipate. This process is called downstream development.

1.3 Northern Annular Mode

Especially in winter time, the strength of the momentum fluxes in baroclinic eddies in the storm track is highly correlated with the northern annular mode (NAM) index. The NAM-index is a zonal index, which is determined by the differences in sea-level pressure in the subtropics and the midlatitudes (Rossby, 1939). Li and Wang (2003) modified the definition of the zonal index to 'the normalized difference in zonal-averaged sea level pressure anomalies between 35°N and 65°N'. The normalisation was done by division by the standard deviation. These specific latitudes are taken, because the anticorrelation of the surface pressure anomaly between these latitudes has a maximum (Lorenz, 1951; Li and Wang, 2003).

In the oscillation of the NAM, we can define two phases. In the positive phase, the surface pressure is relatively high at low latitudes and relatively low at high latitudes. This phase is associated with strong surface westerlies. In Northern Europe, the positive NAM phase corresponds in winter with mild temperatures and more than average precipitation. In the negative phase, the surface pressure difference between subpolar and subtropics is much smaller than in the positive phase with relatively high surface pressures at high latitudes and relatively low surface pressures

at low latitudes. This phase is associated with blocking and corresponds in Northern European winter with dry and cold weather.

A different representation of the same oscillation as the NAM is the Arctic Oscillation (AO) (Thompson and Wallace, 1998). The AO is based on the first empirical orthogonal function of the complete spatial field, whereas the NAM is based on zonal averages. By studying one ocean basin only instead of the zonal averaged circulation, one can also define regional oscillation indices. The North Atlantic Oscillation (NAO) is a local oscillation that shows a similar pattern as the NAM (Walker, 1924; Wallace and Gutzler, 1981). In the early 2000's, a discussion took place in the literature on the question whether the preferred index should be the NAM-index or the NAO-index (Wallace, 2000; Ambaum et al., 2001). Thompson and Wallace (2000) stated that the NAO and Pacific North America pattern (PNA) are local manifestations of the AO, where the NAO has the strongest influence on the complete hemisphere. Ambaum et al. (2001) favour the use of the NAO. In their view, the NAO is more physically relevant and robust for the northern hemisphere variability than the AO.

In this thesis, we will look at the NAM. By zonally averaging, the general circulation can be split in a zonal average zonal circulation, a zonal average meridional circulation and asymmetries on top of those two. Furthermore, we can base a theory for the NAM on physical quantities, such as zonal averages.

1.4 The isentropic coordinate system

In atmospheric modelling and data analysis, different vertical coordinates are used. The most common coordinate systems have either z, the real height (in m), or p, the pressure (in hPa), or θ, the potential temperature (in K) as a vertical coordinate. We will perform most of our analyses with the isentropic coordinate system. An advantage of the isentropic coordinate system is the clear distinction between diabatic and adiabatic processes. In adiabatic circumstances, the potential temperature is conserved, from which follows that mass fluxes are parallel to isentropes. Diabatic heating or cooling is necessary for cross-isentropic mass fluxes.

In the isentropic coordinate system, the heat transport is manifested as a mass flux. The isentropic meridional mass flux (MMF) is given by

$$\text{MMF} = v\sigma \tag{1.8}$$

where v is the meridional velocity and σ is the isentropic density, which can be calculated by

$$\sigma \equiv -\frac{1}{g}\frac{\partial p}{\partial \theta} \tag{1.9}$$

where g is the gravitational acceleration, p is the pressure and θ is the potential temperature.

In Figure 1.2, the zonal mean MMF and zonal mean pressure are plotted averaged over all January months from 1979–2016 and for all latitudes ranging from 70°S up to 70°N. In the figure we can clearly see the winter Hadley circulation between the equator and 25°N, with a poleward branch centring around 340 K and an equatorward return flow between 290 K and 310 K. Only the winter Hadley cell is visible in the figure. On the summer side of the equator, the Hadley circulation is very weak. In the midlatitudes on the northern hemisphere, baroclinic eddies cause a poleward mass flux centred around 300 K and an equatorward return flow with a maximum at 280 K. The eddy activity is the most intense in the winter hemisphere. In the southern hemisphere summer, the mass fluxes in the midlatitudes are of lower amplitude than the mass fluxes in the northern hemisphere winter.

Momentum fluxes in the isentropic coordinate system are represented by fluxes of potential vorticity substance (PVS). The PVS flux has only isentropic components and no cross-isentropic terms, which means that isentropes are impermeable to PVS. This is known as the 'impermeability theorem for potential vorticity substance'. The meridional isentropic potential vorticity substance flux (MPF) is given by

$$\text{MPF} = v\zeta_{abs} \tag{1.10}$$

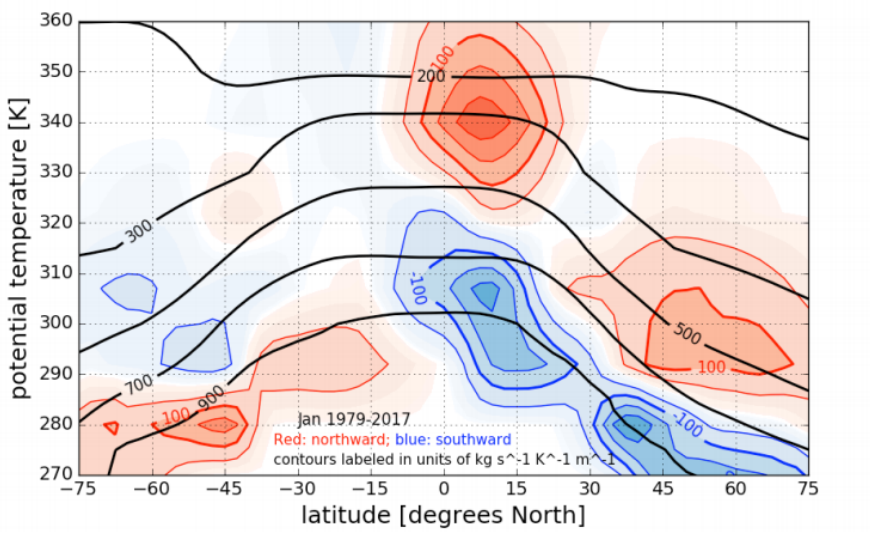

Fig. 1.2: Ensemble monthly mean, zonal mean isentropic mass flux as a function of potential temperature (the vertical coordinate) and latitude, for January in the period 1979–2016. Red contours and shading corresponds to a northward mass flux. Blue contours and shading corresponds to a southward mass flux. Contours are drawn at 50 kg s^{-1} K^{-1} per metre in longitude intervals. Shading starts at ±5 kg s^{-1} K^{-1} per metre in longitude. Black contours represent lines of constant pressure (isobars), labeled in hPa. Source of the data: ERA-Interim (`http://apps.ecmwf.int/datasets/data/interim-full-daily/levtype=pt/`). Figure and caption are taken from van Delden (2017).

where ζ_{abs} is the absolute vorticity on an isentrope, given by

$$\zeta_{abs} = f + \zeta_{rel} = f + \left(\frac{\partial v}{\partial x} - \frac{\partial u}{\partial y}\right)_\theta \tag{1.11}$$

where ζ_{rel} is the relative vorticity on an isentrope and u is the eastward velocity.

By using Kelvin's circulation theorem, which states that absolute circulation is conserved, we can give a relation between the MPF and the zonal mean zonal wind $[u]$ at a certain latitude ϕ, according to

$$[u]_\phi(t) \propto \int_{t_0}^{t} [v\zeta_{abs}]_\phi \, dt' \tag{1.12}$$

This relation implies that a poleward MPF at latitude ϕ leads to an increase in the zonal mean zonal wind at latitude ϕ. Equatorward MPF leads to a decrease in the zonal mean zonal velocity.

As seen in the previous paragraph, fluxes can be studied by looking at the zonal mean circulation. These total zonal mean fluxes can be split in a mean part and an eddy part according to

$$[vX] = [([v] + v^*)([X] + X^*)] = [v][X] + [v^*X^*] \tag{1.13}$$

where X is a dummy variable which e.g. represents a chemical tracer, mass or absolute vorticity. The square brackets represent a zonal average, i.e. an average over all longitudes along a latitude circle. The first term $[v][X]$ is the mean part of the circulation and the second term $[v^*X^*]$ is the eddy part of the circulation.

1.5 MMF and MPF in reanalysis data

Recent research has shown that the monthly average NAM-index in January is strongly correlated with the isentropic meridional mass flux in baroclinic waves at 50°N and on the 307.5 K isentrope

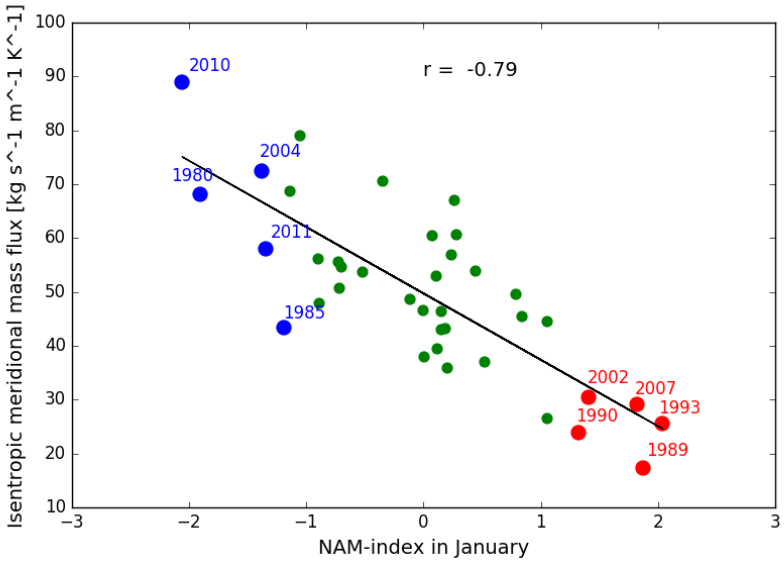

Fig. 1.3: The monthly mean isentropic meridional mass flux, in the layer between $\theta = 285$ K and $\theta = 315$ K at 50°N in January of the years 1979 to 2016, as a function of the monthly mean NAM-index, as defined by Li and Wang (2003), based on the ERA-Interim reanalysis of January 1979-2016 (`http://apps.ecmwf.int/datasets/`). The NAM-index and the northward mass flux at 50°N are anti-correlated. The square of the correlation coefficient, is 0.62, which means that 62% of the variance in the data is explained by the straight line. The extreme years, in terms of NAM-index, are indicated explicitly. The relation between NAM-index and meridional isentropic mass flux is most robust for extreme positive NAM-index. Figure and caption are taken from van Delden (2018).

(Figure 1.3). The analyses are performed with ERA-interim reanalysis data (Dee et al., 2011). In winters in which the NAM-index is strongly negative, the highest mass fluxes are observed. For winters with a positive NAM-index, the isentropic mass fluxes are much weaker. A reasonable explanation for this negative correlation is the fact that enhanced poleward mass flux at a certain latitude ϕ leads to the presence of more mass northward of latitude ϕ. More mass leads automatically to a higher average surface pressure northward of latitude ϕ and with that to a decreased difference in surface pressure between high and low latitudes, which can be seen in a low NAM-index. For reduced mass fluxes, this is exactly opposite and leads thus to a high NAM-index.

By looking at the longitudinal dependence of the MMF, we can distinguish two different regimes. In Figure 1.4, a Hovmöller diagram of the total MMF in the layer between 300 K and 315 K at 50°N is given for the January months of 2007 and 2010. The NAM index was very positive in January 2007 and very negative in January 2010. In the beginning of January 2007, the MMF bulges have a high propagation speed to the east. The most intense signal is found over the Pacific and Atlantic basin. Over the Eurasian continent, the MMF is lower than over the ocean basins. The corresponding zonal averaged MMF is low in this period. From day 19, the MMF bulges slow down and become more stationary. The shift in propagation speed corresponds to a shift to a more negative phase of the NAM index. The slow down of the eastward waves originate from the Pacific region and this information is transported eastward to the Atlantic basin. The pattern in January 2010 is more like the pattern at the end of January 2007, with a relatively low eastward propagation speed. The corresponding zonal averaged MMF is high for this month. A negative NAM phase thus corresponds to a stationary MMF pattern, with high zonal averaged MMF. The positive NAM phase corresponds to a transient MMF pattern, with low zonal averaged MMF.

The positive and negative NAM phases can also be distinguished in the MPF pattern, see Figure 1.5. The zonal average eddy MPF is plotted for January 2007 and January 2010. In the

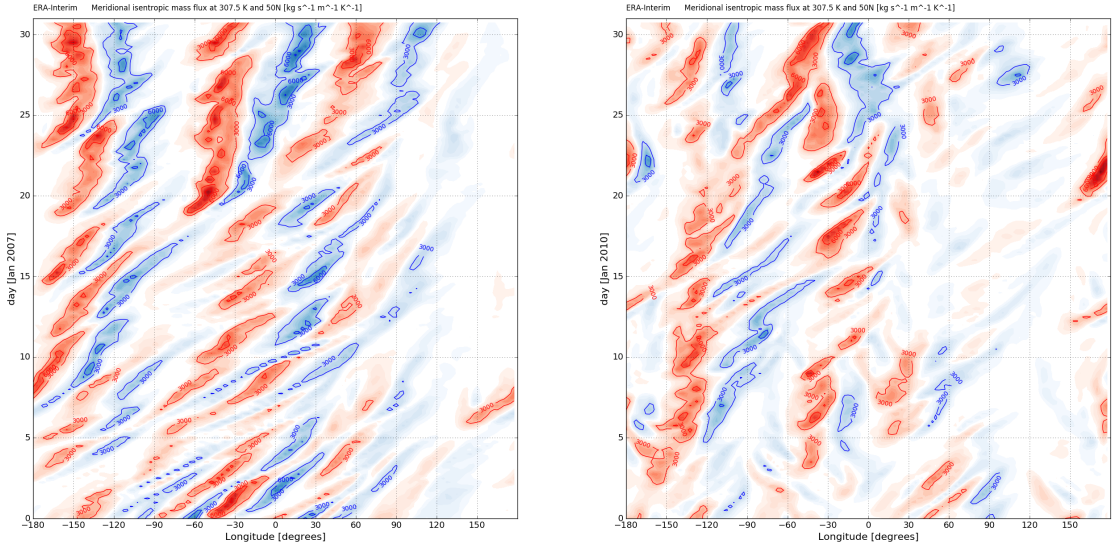

(a) January 2007 *(b)* January 2010

Fig. 1.4: Total meridional isentropic mass flux at 50°N in the layer between 300 K and 315 K. The isentropic mass flux is given in kg m^{-1} K^{-1} s^{-1}. Red contours correspond to northward mass transport, blue contours to southward mass transport. The contour interval is 3000 kg m^{-1} K^{-1} s^{-1} and shading starts at 1000 kg m^{-1} K^{-1} s^{-1}. The MMF is plotted for the months Januay 2007 (a) and January 2010 (b). The data is taken from the ERA-interim reanalysis.

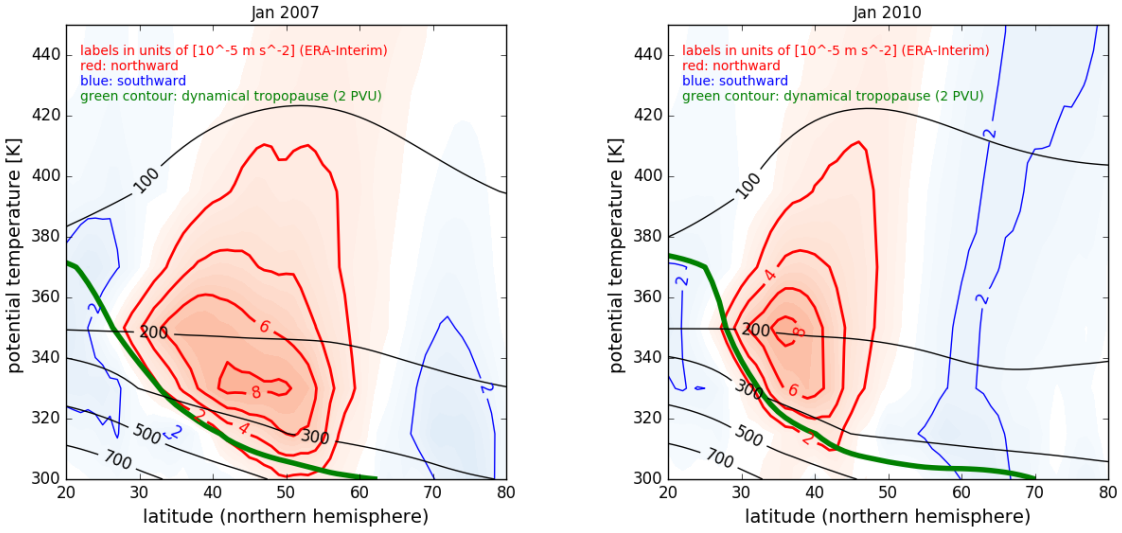

(a) January 2007 *(b)* January 2010

Fig. 1.5: Monthly mean, zonal mean eddy isentropic PVS-flux in January 2007 (a) and in January 2010 (b) (van Delden, 2018). The eddy MPF is given in 10^{-5} m s^{-2}. Red shading corresponds to northward eddy MPF, which in adiabatic circumstances should lead to acceleration of the zonal mean zonal wind. Blue shading corresponds to southward eddy MPF, which in adiabatic circumstances should lead to deceleration of the zonal mean zonal wind. Also shown is the monthly mean, zonal mean pressure distribution (black contours, labeled in hPa) and the dynamical tropopause (green), which corresponds to the 2 potential vorticity units contour.

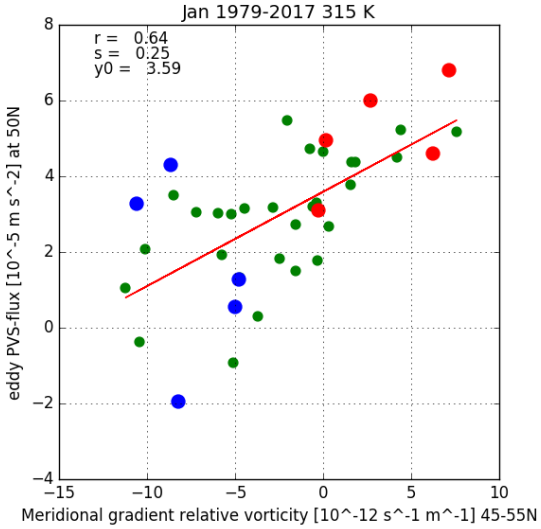

Fig. 1.6: Scatter plot of the monthly mean values of the zonal mean eddy MPF, at 315 K and 50°N, in January (1979–2017), and the corresponding zonal mean meridional gradient of relative vorticity, at 315 K and 50°N, calculated by taking the difference of the relative vorticity at 45°N and 55°N and dividing by the distance between these two parallels. The meridional gradient of planetary vorticity at 50°N is $\beta = 14.7 \cdot 10^{-12}$ m^{-1} s^{-1}. The red dots represent the 5 months with extreme positive NAM-index (van Delden, 2018, Figure 11). The blue dots represent the 5 months with extreme negative NAM-index (van Delden, 2018, Figure 11). The correlation coefficient of the linear fit to all the dots is 0.64. Figure and caption taken from van Delden (2018).

positive NAM month, the northward eddy MPF is spread over a larger latitudinal band, namely from 30 – 60°N, than in the negative NAM month, where it is confined to a 30 – 50°N. North and south of the northward eddy MPF bulge, the eddy MPF is southward. According to Equation 1.12, northward MPF accelerates the zonal mean zonal wind, whereas southward MPF decelerates the zonal mean zonal wind. In both months the zonal mean zonal wind is accelerated by the eddies in the midlatitudes and the zonal mean zonal wind is decelerated by the eddies at high and low latitudes. We should note, however, that most of the eddy MPF activity takes place in the stratosphere. In the rest of this thesis, we will look at tropospheric processes. The strong signals as found in the reanalysis data are therefore not expected in our analyses.

A remarkable relation between the MPF and the vorticity gradient was found by van Delden (2018). Normal turbulence theory prescribes a negative correlation between a flux of some substance with its gradient. Fluxes are down-gradient in this theory. In Figure 1.6, the relation between the zonal mean eddy MPF and the meridional gradient of relative vorticity are given for January (1979–2017). On the horizontal axis, the relative vorticity is given. To obtain the absolute vorticity, the latitudinal variation in the Coriolis parameter, β, should be added to the values given on the horizontal axis. The absolute vorticity gradient is positive for all January months and the correlation between these two variables is positive. By looking at the positive NAM months, the correlation is stronger than for the negative months. The up-gradient transport of eddy MPF is associated with a phenomenon called negative viscosity (Starr, 1968).

1.6 Research questions

We want to study the processes that determine the isentropic meridional mass fluxes and with that we want to understand the causes of the high and low NAM phases. Because most of the meridional mass transport in the midlatitudes is caused by baroclinic eddies, we will look at meridional mass fluxes in baroclinic eddies. We will especially study the poleward branch of the

MMF. In the isentropic coordinate system, the poleward branch of the midlatitude MMF can be analysed properly without taking into account diabatic effects. The equatorward return flow 'hits' the Earth's surface and is captured in the underworld. Only diabatic effects lead to cross isentropic fluxes, which return the flow to the equator.

For this thesis, we will simulate baroclinic life cycles with an idealised model. In different simulations, we tune a variety of model parameters and initial conditions to study the sensitivity of the modelled baroclinic waves to the different parameters. The sensitivity study helps us in understanding the physical processes behind the variation of the Northern Annular Mode. With a reference to Figure 1.2, we want to understand all fluxes that are visible in the data. Which fluxes are caused by baroclinic eddy activity? Which processes cause a high MMF?

In Chapter 2, a more elaborate description of the model is given. In Chapter 3, the results of different model runs are shown. Chapter 4 discusses the implication of the results and the restrictions of the model used. Finally, Chapter 5 gives the conclusions of this research and gives an outlook to further research.

2. MODEL DESCRIPTION

To simulate the life cycle of a baroclinic wave, we used a primitive equation model. The basis of the model is a closed set of equations, which is referred to as primitive equations. The model is written in σ-coordinates, where the levels are expressed as a fraction of the surface pressure. σ runs from 0 to 1, where $\sigma = 0$ corresponds to $p = 0$ and $\sigma = 1$ corresponds to $p = p_s$. In this grid point model, the convergence of meridians to the north is neglected, which implies that the grid spacing is constant over the complete domain. The model is simplified to a β-plane model, where the Coriolis parameter is approximated by $f = f_0 + \beta y$. f_0 and β are taken at the central latitude $\phi_0 = 45°$N with a value of $f_0 = 2\Omega \sin(45°) \approx 1.035 \cdot 10^{-4}$ s^{-1}and $\beta = 2\Omega/a \cos(45°) \approx 1.625 \cdot 10^{-11}$ m^{-1} s^{-1}, where Ω is the angular speed of the Earth's rotation and a is the radius of the Earth. The model equations are written in flux form and are in adiabatic conditions given by (van Delden, 2017)

$$\frac{\partial p_s}{\partial t} + \frac{\partial p_s u}{\partial x} + \frac{\partial p_s v}{\partial y} + p_s \frac{\partial}{\partial \sigma}\left(\frac{d\sigma}{dt}\right) = 0 \tag{2.1}$$

$$\frac{\partial \Phi}{\partial \sigma} = -\frac{RT}{\sigma} \tag{2.2}$$

$$\frac{\partial p_s \theta}{\partial t} = -\left(\frac{\partial p_s u\theta}{\partial x} + \frac{\partial p_s v\theta}{\partial y}\right) - \frac{\partial}{\partial \sigma}\left(p_s \theta \frac{d\sigma}{dt}\right) + \frac{p_s J}{\Pi} \tag{2.3}$$

$$\frac{\partial p_s u}{\partial t} = -\left(\frac{\partial p_s u^2}{\partial x} + \frac{\partial p_s uv}{\partial y}\right) - \frac{\partial}{\partial \sigma}\left(p_s u \frac{d\sigma}{dt}\right) + (f_0 + \beta y)\, p_s v - \left(p_s \frac{\partial \Phi}{\partial x} + RT \frac{\partial p_s}{\partial x}\right) \tag{2.4}$$

$$\frac{\partial p_s v}{\partial t} = -\left(\frac{\partial p_s uv}{\partial x} + \frac{\partial p_s v^2}{\partial y}\right) - \frac{\partial}{\partial \sigma}\left(p_s u \frac{d\sigma}{dt}\right) - (f_0 + \beta y)\, p_s u - \left(p_s \frac{\partial \Phi}{\partial y} + RT \frac{\partial p_s}{\partial y}\right) \tag{2.5}$$

$$\frac{\partial p_s}{\partial t} = -\int_0^1 \frac{\partial p_s u}{\partial x} + \frac{\partial p_s v}{\partial y} d\sigma \tag{2.6}$$

In this set of equations, the horizontal velocity (u and v), the vertical velocity ($d\sigma/dt$), the geopotential (Φ), the surface pressure (p_s) and the potential temperature (θ) are the variables to be updated at every time step by the model. The potential temperature can be calculated according to

$$\theta = T\left(\frac{p}{p_{ref}}\right)^{\kappa} \tag{2.7}$$

where T is the temperature, $p_{ref} = 1000$ hPa and $\kappa = R/c_p \approx 0.286$, the gas constant over the heat capacity at constant pressure. The term $p_s J/\Pi$ in Equation (2.3) is the diabatic term, where J is the diabatic heating per unit mass per unit time and Π is the Exner function given by

$$\Pi = c_p\left(\frac{p}{p_{ref}}\right)^{\kappa} \tag{2.8}$$

The diabatic heating and cooling in the model is given by a simple parametrisation of radiative flux divergence as

$$\frac{\partial T}{\partial t} = -\alpha_N (T - T_R) \tag{2.9}$$

where α_N is the Newtonian cooling coefficient and T_R is the radiative determined temperature, which is the initial model state. The inverse of the Newtonian cooling coefficient gives a time scale

on which the system returns back to the original state. The real time scale of a baroclinic life cycle is 5 – 10 days, which corresponds to a Newtonian cooling coefficient in the order of 10^{-6} s^{-1}.

The advection, pressure gradient and Coriolis term are approximated with the MacCormack scheme, which is a predictor–corrector scheme (Mendez-Nunez and Carroll, 1993). The surface pressure equation is solved using centred differences in space and the same predictor–corrector scheme as in the MacCormack scheme in time (van Delden, 2017). The model time step is 10 seconds. Every three hours of model time, the fields of p_s, $p_s u$, $p_s v$ and $p_s \theta$ are smoothed using a horizontal five-point smoother.

The simulations are performed with a primitive equation model with 25 layers in the vertical (PeN25-model). The horizontal domain has the shape of a channel of 360° in longitude with periodic boundary conditions in east-west direction and 90° in latitude with open boundaries on the north and south side. The horizontal spacing is divided in 288 points in x-direction ($\Delta x = 1.25°$) and in 101 points in y-direction ($\Delta y = 0.9°$).

In the initial situation the geopotential is given by (van Delden, 2017)

$$\Phi(x, y, p, t = 0) = \Phi_0(p) - y_{scale} f_0 U_0 \tanh\left(\frac{y - y_0}{y_{scale}}\right) \cos\left(\frac{\pi p}{2p_0}\right) \tag{2.10}$$

where Φ_0 is the geopotential at $y = y_0$, the central latitude, y_{scale} is the width of the temperature front and the associated jet and U_0 the maximum wind speed in the associated jet. The surface pressure is initially prescribed as a homogeneous field with a value of 1000 hPa. The geopotential at $y = y_0$ can be calculated from the integration of the hydrostatic equation. To be able to perform this integration, we need the temperature at the central latitude T_0, which is given by

$$T_0(z) = T_0(z = 0) - \Gamma_0 z \tag{2.11}$$

where $T_0(z = 0) = 285$ K and Γ_0 is the temperature lapse rate. In the model, the temperature lapse rate is a model parameter which is constant during a model run.

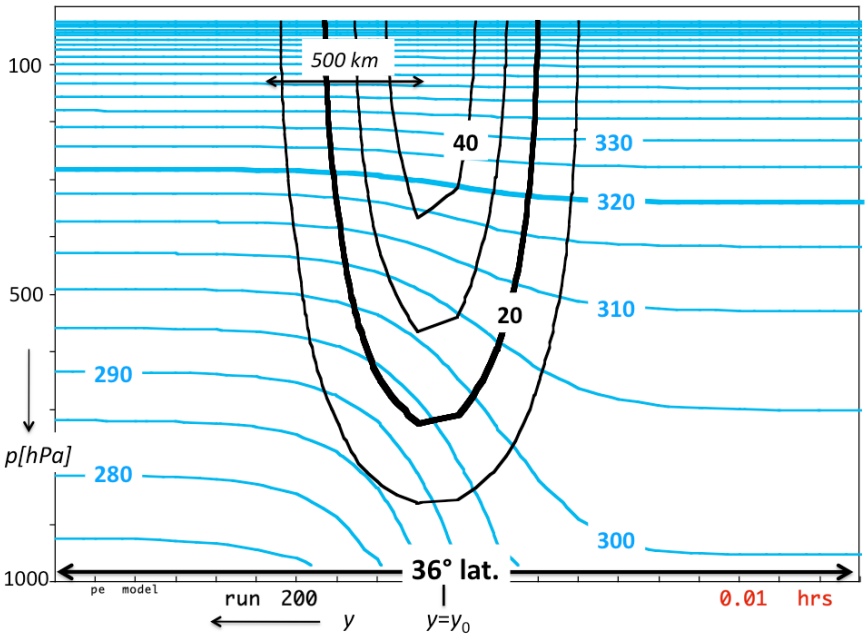

Fig. 2.1: Geostrophic zonal wind with $U_0 = 50$ m s^{-1} and $y_{scale} = 500$ km, and potential temperature, according to thermal wind balance, as a function of latitude and pressure at initial time in the model. Labels are indicated in m s^{-1} and K, respectively. Figure and (modified) caption taken from van Delden (2017).

From the geostrophic balance, the geostrophic jet can be calculated from the geopotential according to

$$u_g(x, y, p, t = 0) = U_0 \cos\left(\frac{\pi p}{2p_0}\right)\left(1 - \tanh^2\left(\frac{y - y_0}{y_{scale}}\right)\right) \tag{2.12}$$

The temperature at every latitude can be calculated by using the thermal wind equation. Figure 2.1 gives the initial distribution of the potential temperature θ and zonal wind u in the model.

The zonal structure of the initial flow field is perturbed by making the reference latitude dependent on longitude, according to

$$\phi_0(x) = \phi_{00} + C \sin\left(\frac{2\pi k x}{L_x}\right) \tag{2.13}$$

where ϕ_0 is latitude around which the front is centred, C is the latitudinal extent of the meandering front and k is the initial wave number. The initial wave number gives the number of waves in the complete domain of the model in the initial meandering front and is a model parameter that can be set at the beginning of the model run.

To sum up, the parameters in the model that are tunable are the temperature lapse rate Γ_0, the width of the front y_{scale}, the strength of the jet U_0, the Newtonian cooling coefficient α_N and the initial wave number k. For this thesis, several model runs are performed with different initial conditions and different model parameters.

The raw model output, which is vertically calculated at σ-levels, is interpolated to pressure or isentropic levels for analysis. If the vertical coordinate is pressure, the velocities, geopotential and potential temperature at each level are saved. If the vertical coordinate is potential temperature, the velocities, isentropic density and pressure are saved at all levels. The analysis of the results is discussed in Chapter 3.

3. RESULTS

3.1 Initial conditions

We performed different runs with the 25 level model with different initial conditions. The model parameters were the same during all runs: $\Gamma = 6.5$ K km^{-1}, $\alpha_N = 1.0 \cdot 10^{-6}$ s^{-1}, $y_{scale} = 500$ km, $U_0 = 50$ m s^{-1}. The difference is the initial zonal wave number k. A first remarkable result that follows from the simulation, is that the initial condition of the model is important for the solution.

Although all runs are initially baroclinically unstable, the runs behave differently after the first development of a baroclinic wave. In Figure 3.1, the surface pressure, potential temperature and wind vectors at the 850 hPa level are plotted for $k = 5$ and $k = 6$ at day 21.75. In the run with $k = 5$ (Figure 3.1a), a wave train of low pressure systems develops after the first few baroclinic life cycles. Eventually, the wave number doubles to 10. The final situation is an approximately statistically stable situation, in which the low pressure systems are advected eastward. During the advection no growth and decay of new baroclinic unstable situations occurs. In the run with $k = 6$ (Figure 3.1b), new waves grow in amplitude. A new low pressure system grows and the established low pressure system decays. The process of growth and decay is visible during the complete model run. The run with $k = 4$ has, after an initial development of baroclinic life cycles, also a doubling of the initial wave number, which is similar as in $k = 5$. During the run with $k = 7$, new baroclinic life cycles develop. The mass fluxes corresponding to these life cycles are weaker than for $k = 6$.

In Table 3.1, the wave lengths corresponding to the different wave numbers k are given. In Figure 3.2, the results of the stability analysis of Phillips (1954) is shown with the parameters used in the 25 layer primitive equation model. Furthermore, the condition of the model is given at different times for the runs with $k = 5$ and $k = 6$. Initially, all model solutions are unstable with a shear of 3.2 m s^{-1} km^{-1} averaged between 250 hPa and 750 hPa. After the first few baroclinic life cycles, the shear has decreased to 1.4 m s^{-1} km^{-1} averaged between 250 hPa and 750 hPa. Wave numbers $k = 6$ and $k = 7$ seem still unstable during the complete model run, where $k = 6$ is the fastest growing mode. However, according to the theory of Phillips, the shear is too low to have an unstable situation. An explanation for the disagreement between the theory and the results could be that Phillips' theory, which is designed for a two layer model, is not one-to-one translatable to a 25 layer model. Wave numbers $k = 4$ and $k = 5$ are doubled during the model runs. The wave numbers $k = 8$ and $k = 10$ have a too short wave length for unstable solutions.

To study the MMF in the runs with $k = 5$ and $k = 6$ in more detail, a time average of the zonal average total isentropic mass flux is plotted in Figure 3.3. We see that around 300 K and 45°N a bulge of northward mass flux is visible in all simulations. The northward mass transport is compensated by a southward mass transport in the lowest layer of the atmosphere. The circulation

Wave number k	Wave length
4	$8.8 \cdot 10^3$ km
5	$7.1 \cdot 10^3$ km
6	$5.9 \cdot 10^3$ km
7	$5.1 \cdot 10^3$ km
8	$4.4 \cdot 10^3$ km
10	$3.5 \cdot 10^3$ km

Tab. 3.1: The wave lengths of the baroclinic waves corresponding to the different wave numbers.

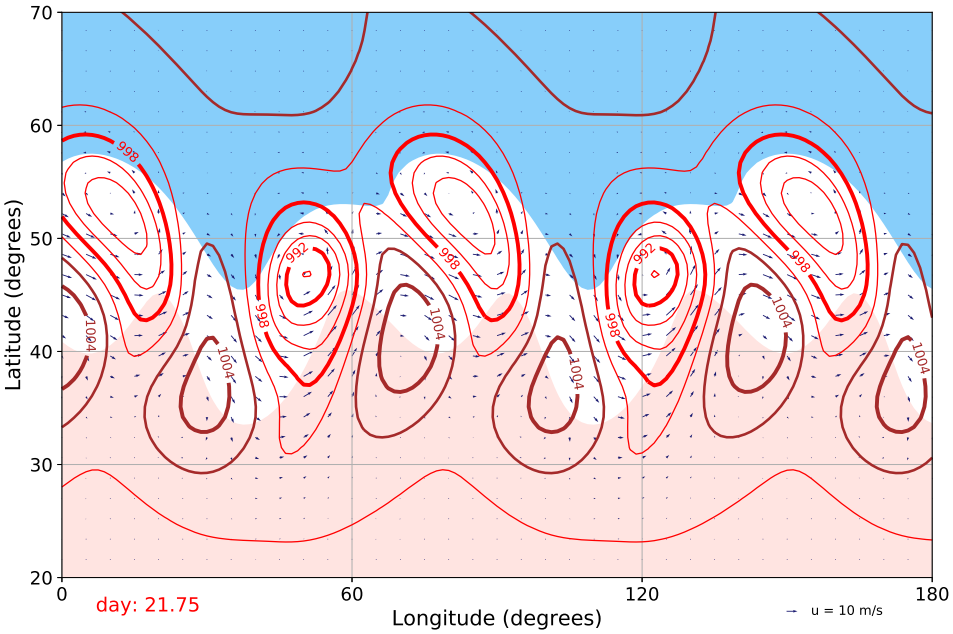

(a) $k = 5$

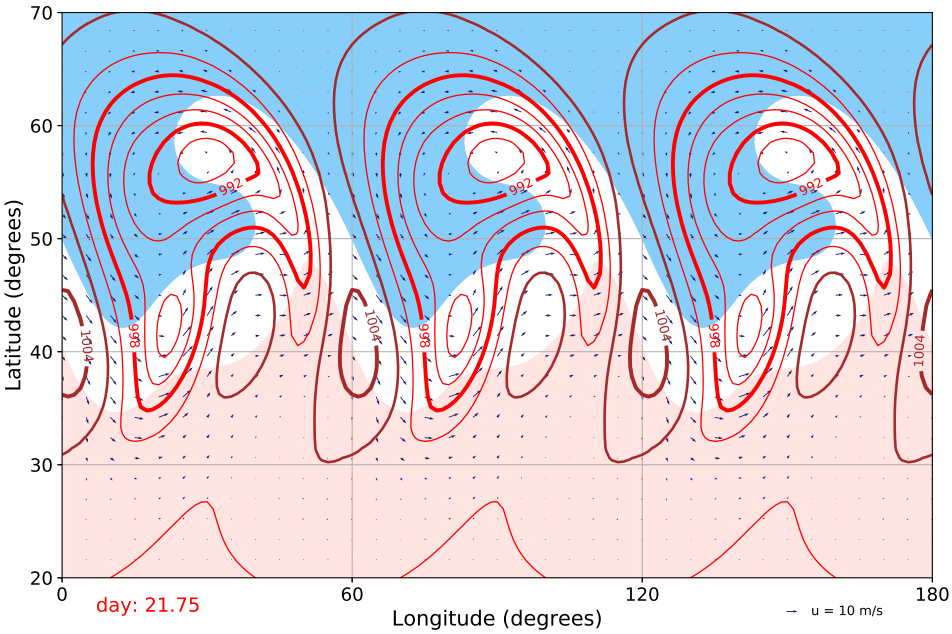

(b) $k = 6$

Fig. 3.1: Surface pressure (red and brown contours), potential temperature (red and blue shading) at the 850 hPa level and wind vectors at the 850 hPa level at day 21.75 in a part of the domain. The surface pressure is plotted in hPa with a contour interval of 2 hPa, where red contours are used for $p \leq 1000$ hPa and brown contours are used for $p \geq 1002$ hPa. Red shading is used for $\theta \geq 295$ K and blue shading is used for $\theta \leq 285$ K. In these runs, $\Gamma_0 = 6.5$ K km^{-1}, $y_{scale} = 500$ km, $U_0 = 50$ m s^{-2} and $\alpha_N = 1.0 \cdot 10^{-6}$ s^{-1}. The initial wave number k is different for both runs.

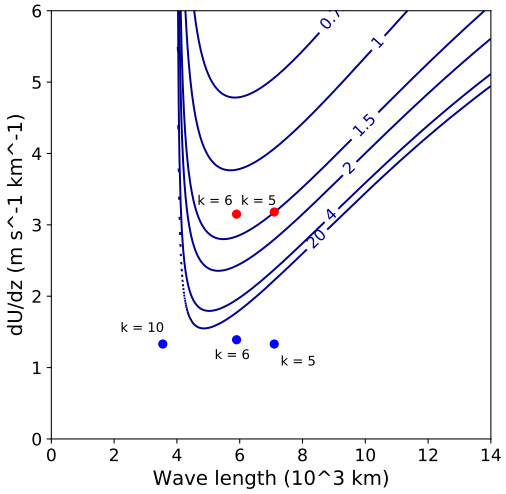

Fig. 3.2: The time in days required for an unstable wave in the two-level model to double its amplitude, given as a function of the vertical wind shear in the basic current and the wavelength as calculated from citetphillips1956 with the parameters used in our PeN25 model. The dots represent the state of the PeN model during a certain run and time. The upper red dots are the conditions at $t = 3$ hours for $k = 5$ and $k = 6$, the lower blue dots are averages over $t = 1200 - 1500$ hours for $k = 5$ and $k = 6$. A dot for the wave length corresponding to $k = 10$ is also given, because the $k = 5$ run doubles its wave length.

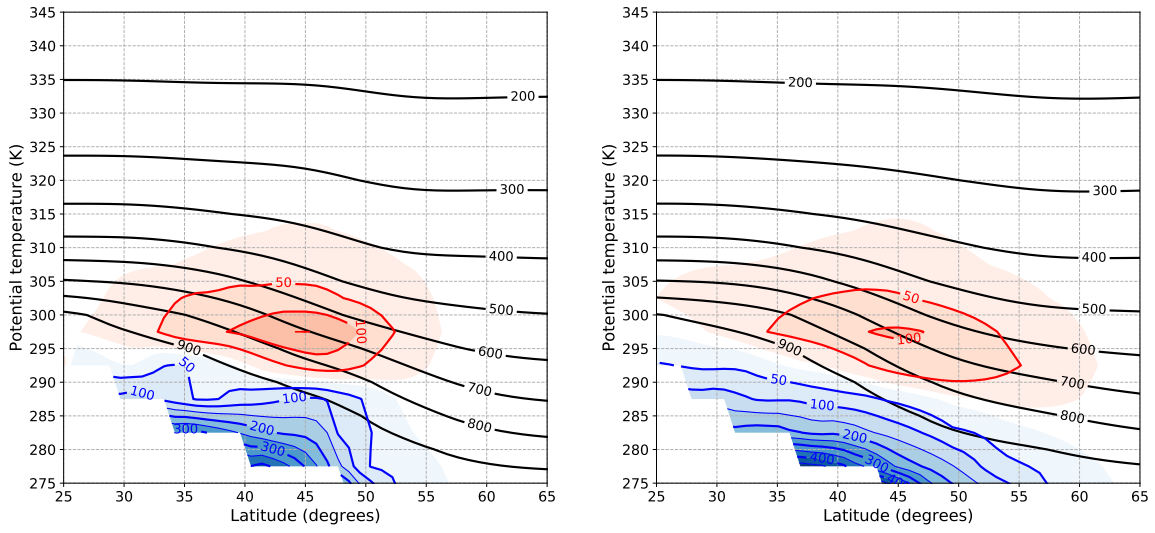

(a) $k = 5$ *(b)* $k = 6$

Fig. 3.3: Zonal mean time mean total isentropic mass flux (red and blue contours) and zonal mean pressure (black contours) for different initial wave numbers. The zonal mean isentropic mass flux is plotted in kg m^{-1} K^{-1} s^{-1}. Red is northward flux, blue is southward flux. The shading starts at 10 kg m^{-1} K^{-1} s^{-1}. The zonal mean pressure is plotted in hPa. The time average is taken over model days 30 – 60. The model parameters are the same as in Figure 3.1.

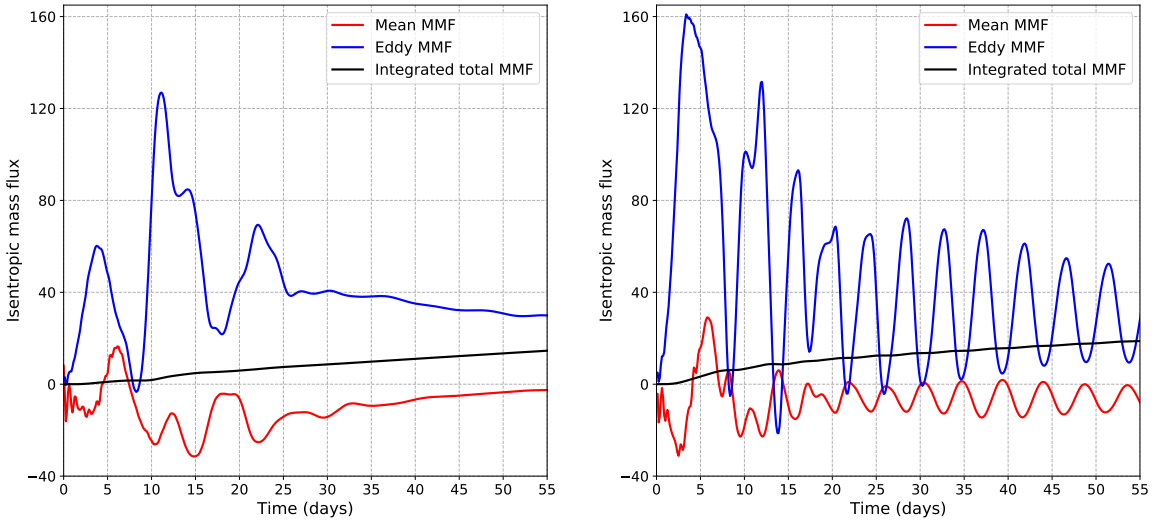

(a) $k = 5$ *(b)* $k = 6$

Fig. 3.4: Zonal mean isentropic mass flux at 307.5 K and 45°N. The isentropic mass flux is split into a mean part (red) and an eddy part (blue), both given in kg m^{-1} K^{-1} s^{-1}. In black, the integrated total isentropic mass flux is given in 10^7 kg m^{-1} K^{-1}. Positive values correspond to northward mass transport, negative values to southward mass transport. The model parameters are the same as in Figure 3.1.

and the magnitude of the mass fluxes are comparable to the MMF found in the reanalysis data as shown in Figure 1.3. In the more statistically stable situation, model days 30 – 60, the northward mass flux is higher in the run with $k = 5$. The northward mass transport is, however, spread over a larger range of latitudes for $k = 6$.

By looking at time series (Figure 3.4), the difference between the runs can be visualised. The mean MMF is negatively correlated with the eddy MMF. For $k = 5$, the model run starts with 3 events of 8 – 9 days in which a northward eddy MMF reduces the baroclinicity. After these 3 events, both the mean and eddy MMF are approximately constant. The constant MMF belongs to the state in which almost no growth and decay of low pressure systems occurs. During this stage, the MMF is necessary to compensate the restoring mechanism of the Newtonian cooling. The compensation occurs at the same rate as the restoration, so no net baroclinicity is built up.

After an initial stage in the run with $k = 6$, the baroclinicity is recovered enough to sustain growth and decay of low pressure systems. The eddy MMF has northward pulses with a period of 4 – 5 days and the mean MMF compensates this with southward pulses, which are smaller in amplitude. The amplitude of the oscillation slowly decays towards the end of the run. The cyclic behaviour between baroclinicity and MMF, or in pressure coordinates heat flux, was studied by Ambaum and Novak (2014), who compared this behaviour with a simple predator-prey model.

The longitudinal dependence of the MMF is shown in a Hovmöller diagram in Figure 3.5. We see that the solution is translational symmetric. The difference between $k = 5$ and $k = 6$ becomes very clear after the initial 'start up' phase. Two regimes seem to exist. In Figure 3.5a, the doubling of the initial wave number is clearly visible. This regime consists of relatively fast propagating waves with a constant amplitude. No growth and decay of baroclinic life cycles is visible in the Hovmöller diagram. A positive NAM-phase shows a similar pattern (see Figure 1.4a), with fast propagating low pressure systems. The second regime (Figure 3.5b) shows a regime with a more stationary pattern. Baroclinic life cycles grow and decay with a time period of about 4 days and have a lower eastward propagation speed. This regime shows similarities with the negative

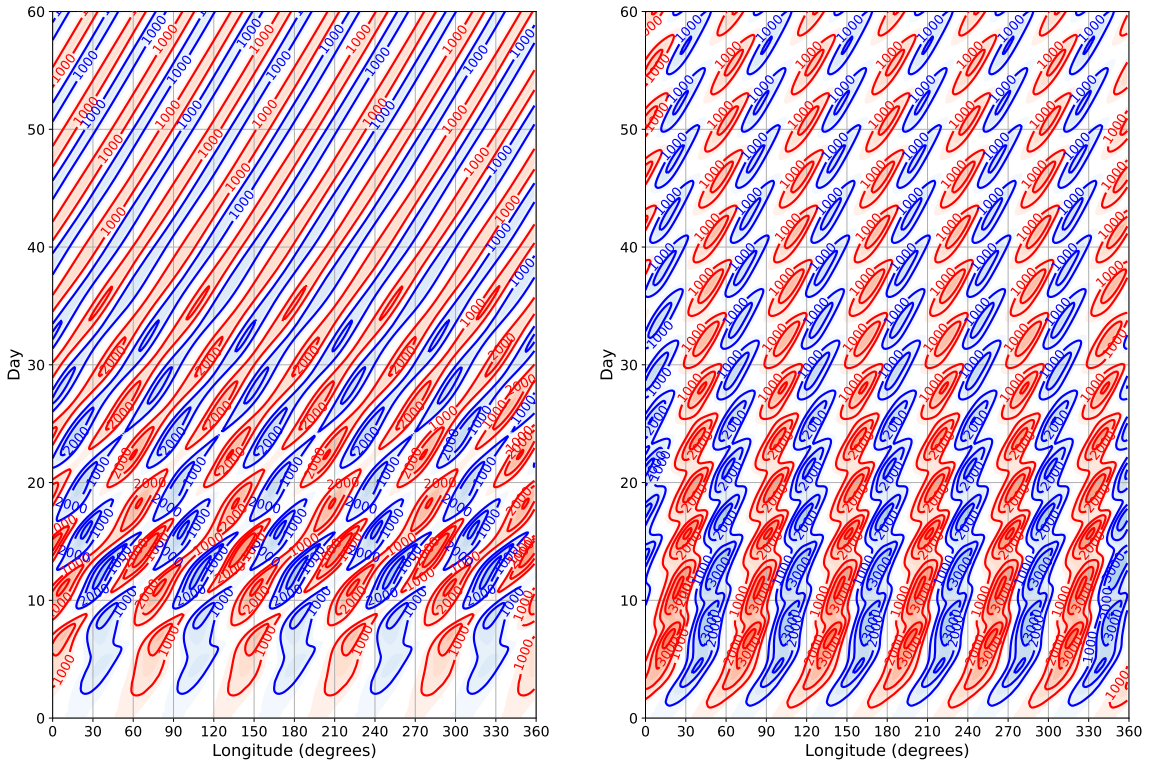

(a) $k = 5$ *(b)* $k = 6$

Fig. 3.5: Total meridional isentropic mass flux at 307.5 K and 45°N. The isentropic mass flux is given in kg m^{-1} K^{-1} s^{-1}. Red contours correspond to northward mass transport, blue contours to southward mass transport. The contour interval is 1000 kg m^{-1} K^{-1} s^{-1} and shading starts at 500 kg m^{-1} K^{-1} s^{-1}. The model parameters are the same as in Figure 3.1.

NAM-phase (see Figure 1.4b), where large bursts of MMF occur at specific locations.

For initial wave number $k = 6$, we see clearly a different phase speed and group speed. The phase speed is $c_x = 5.7$ m s^{-1} and the group speeds is $c_{g,x} = 12.6$ m s^{-1}. The fact that the group speed is higher than the phase speed is in accordance with the theory given in Section 1.2. The exact values can however not be reproduced by the two layer theory. The phase and group speeds are equal for all levels in the atmosphere. The level at which $c_x = [u]$ is called the steering level. In the run with $k = 6$, the steering level is at the central latitude found just above the 290 K isentrope.

For $k = 5$, final situation gives a phase speed of $c_x = 5.1$ m s^{-1}. The group speeds seems equal to the phase speed, as there is no group visible travelling with a different speed. According to the barotropic theory, the group speed and phase speed are equal if the model solution meets the condition in Equation 1.7. U_T is calculated as the difference in zonal mean zonal velocity between 250 hPa and 750 hPa. Initially, $U_T \approx 30$ m s^{-1}. However, the shear decreases relatively quick to final values between 10 and 14 m s^{-1} for the different model runs. The dispersionless condition, which needs U_T to be around 5 m s^{-1}, is not exactly met. However, the solutions of the phase speed and group speed are real between $t = 1200$ hours and $t = 1500$ hours for $k = 5$, whereas the solutions contain an imaginary part for $k = 6$. The imaginary part of the Rossby wave speed

gives an explanation for the instability of the Rossby wave for $k = 6$. The absence of an imaginary part then gives an explanation for the baroclinically stable regime in the run with $k = 5$.

In Figure 3.6, a time average of the zonal average of eddy potential vorticity substance flux is plotted for model days 10 – 30 and days 30 – 60. By comparing Figures 3.6a and 3.6b, we see that the eddy PVS fluxes are higher for $k = 5$ than for $k = 6$. According to Equation 1.12, the zonal mean zonal velocity $[u]$ increases as a consequence of momentum convergence when the MPF is positive (northward) and decreases as a consequence of momentum divergence when the MPF is negative (southward). We see that the MPF is positive on the south side of the jet and negative on the north side of the jet. This dipole causes a southward shift of the jet, because the jet is accelerated on the south side and decelerated on the north side. The dipole is stronger for $k = 5$ than for $k = 6$. In Figures 3.6c and 3.6d, it can be identified that, at the 295 K isentrope, the jet is located more southward for $k = 5$ than for $k = 6$.

3.2 Newtonian cooling

In the previous section, all model parameters were kept constant and the only variation between model runs was the different initial wave number k. In this section, we will look at variations between model runs with a different Newtonian cooling coefficient α_N. In the standard runs (Section 3.1), the Newtonian cooling coefficient was equal to $\alpha_N = 1.0 \cdot 10^{-6}$ s^{-1}, which corresponds to a response time of the system of 11.6 days. In Figure 3.7, the time average of the zonal average MMF is plotted for $\alpha_N = 0.5 \cdot 10^{-6}$ s^{-1} and for $\alpha_N = 2.0 \cdot 10^{-6}$ s^{-1}. It is clear that the MMF is larger for a higher value of the Newtonian cooling coefficient, which is consistent with reality where a stronger diabatic forcing leads to a higher MMF. The Newtonian cooling forces the system back to its original situation, which is baroclinically unstable. High α_N corresponds to a short time scale, which leads to a stronger forcing than for low α_N. This is consistent with the signal in Figure 3.7.

If the Newtonian cooling coefficient is too low, the system is not able to return to a baroclinically unstable situation. The system then is baroclinically stable and no new baroclinic life cycles develop. For higher α_N, the development of new baroclinic waves is maintained. However, the maximum strength of the MMF-peaks slowly decreases in Figure 3.4b for $\alpha_N = 1.0 \cdot 10^{-6}$ s^{-1}. Probably, a longer run would eventually evolve to the wave train without MMF bursts, but this is not verified. If α_N is a factor 2 higher, the peak height is constant in time, which probably could sustain the growth and decay of baroclinic life cycles for a long time.

3.3 Static stability

In Figure 3.8, the static stability is changed for different runs. These runs are performed on a smaller domain than all other results presented in this chapter. The domain spans over 60° in x-direction ($\Delta x = 0.83°$) and from 10.5°N until 79.5°N in y-direction ($\Delta y = 0.6°$).

We see that for a lower static stability (high temperature lapse rate), the isobars are closer together than for a high static stability. The northward MMF is larger for a lower static stability. In the isentropic coordinate system, the maximum of the northward MMF bulge remains at the same height for both runs. However, in isobaric coordinates, the maximum of the northward MMF bulge is higher in the atmosphere for a lower static stability.

3.4 Front width and strength

To study the influence of the front parameters, runs with different front widths and strengths are performed. By enhancing the front width y_{scale}, the total temperature gradient at the surface becomes larger. A wider baroclinic zone exists. In Figures 3.9a and 3.9b, the strength of the jet U_0 is kept constant, but the width of the front is changed. A narrower front leads to a smaller baroclinic zone. For a wider front, both the total slope and the steepness of the slope are larger. The latitudinal band over which the MMF is spread is wider and the centre of the northward MMF

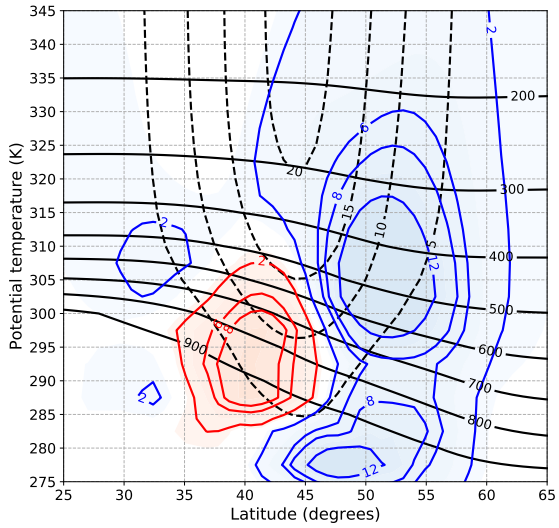

(a) $k = 5$, day 10 – 30

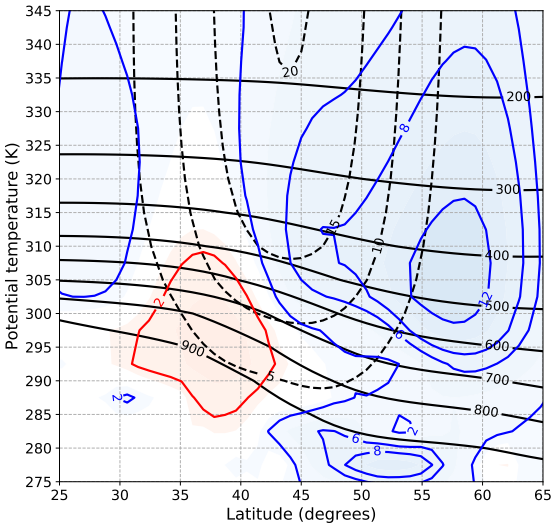

(b) $k = 6$, day 10 – 30

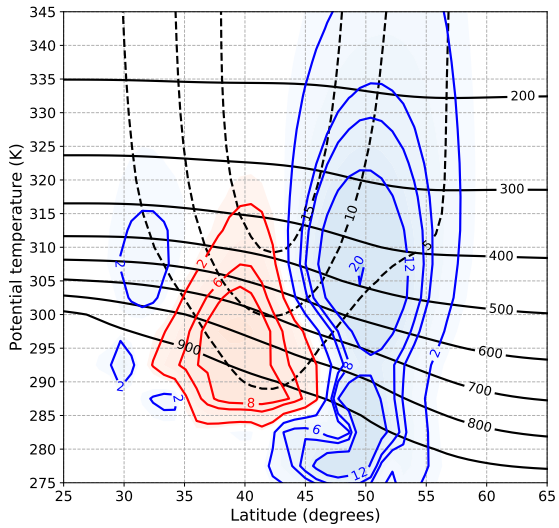

(c) $k = 5$, day 30 – 60

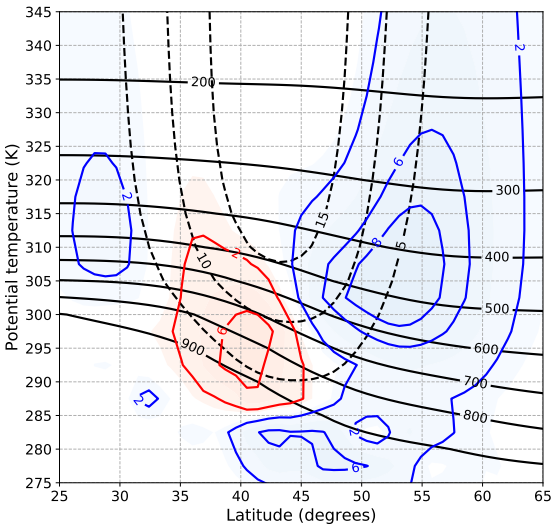

(d) $k = 6$, day 30 – 60

Fig. 3.6: Zonal mean time mean eddy PVS flux (red and blue contours), zonal mean pressure (black contours) and zonal mean zonal velocity (dashed contours) for different initial wave numbers and different time frames. The zonal mean PVS flux is plotted in 10^{-6} m s^{-2}. Red is northward flux, blue is southward flux. The shading starts at 1 m s^{-2}. The zonal mean pressure is plotted in hPa and the zonal mean zonal velocity is plotted in m s^{-1}. The model parameters are the same as in Figure 3.1.

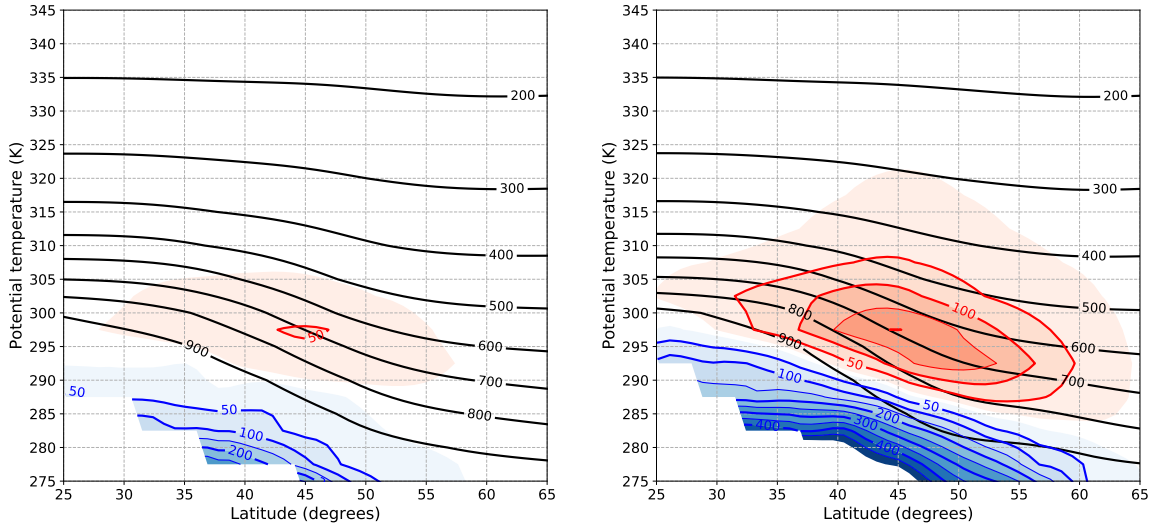

(a) $\alpha_N = 0.5 \cdot 10^{-6}$ s^{-1} (b) $\alpha_N = 2.0 \cdot 10^{-6}$ s^{-1}

Fig. 3.7: Zonal mean time mean total isentropic mass flux (red and blue contours) and zonal mean pressure (black contours) for different initial wave numbers. The zonal mean isentropic mass flux is plotted in kg m^{-1} K^{-1} s^{-1}. Red is northward flux, blue is southward flux. The shading starts at 10 kg m^{-1} K^{-1} s^{-1}. The zonal mean pressure is plotted in hPa. The time average is taken over model days 30 – 60. In these runs, $\Gamma_0 = 6.5$ K km^{-1}, $y_{scale} = 500$ km, $U_0 = 50$ m s^{-2} and $k = 6$. The Newtonian cooling coefficient α_N is different for both runs.

bulge is higher in the atmosphere. The strength of the maximum MMF seems not influenced by the width of the baroclinic zone.

In Figures 3.9c and 3.9d, the slope of the isentropes is kept constant, by keeping the product $y_{scale}U_0$ constant. Figure 3.9c shows a wider front ($y_{scale} = 600$ km) with a weaker jet ($U_0 = 41.67$ m s^{-1}), whereas Figure 3.9d shows a narrower front ($y_{scale} = 400$ km) and a stronger jet ($U_0 = 62.5$ m s^{-1}). We see that the northward MMF is stronger for a narrower and stronger jet. The latitudinal extent as well as the depth of both MMF bulges is similar. Although the baroclinicity is similar in both model runs, the mass flux is strongly influenced by different jet structure. This can be explained by the Eady growth rate (Equation 1.2). By comparing the runs in Figure 3.9c and 3.9d, f and N are similar, but dU_0/dz is larger in Figure 3.9d. The Eady growth rate is thus larger for the stronger jet, which causes a larger MMF than in the weaker jet.

3.5 Longitudinal variations

In all previous sections of this chapter, the boundary conditions were homogeneous. The initial conditions had a translational symmetry that was not broken by the boundaries. In this section, the Newtonian cooling coefficient α_N is not constant over the complete domain. Between 40° and 100° it is four times as high as in the rest of the domain, see Figure 3.10a. During the first 25 days, the system sustains the symmetry. From day 30 the initial growth of baroclinic life cycles still occurs at various latitudes. However, the strongest baroclinic life cycle development occurs in the region with a higher α_N. The baroclinic wave travels eastward to a region where the baroclinicity is recovered at a lower rate. However, the energy of the first decayed life cycle is radiated eastward and is used for the development for the next baroclinic life cycle (Chang and Orlanski, 1993). Downstream of the first baroclinic life cycle, new life cycles grow, decay, are advected and repeat this cycle.

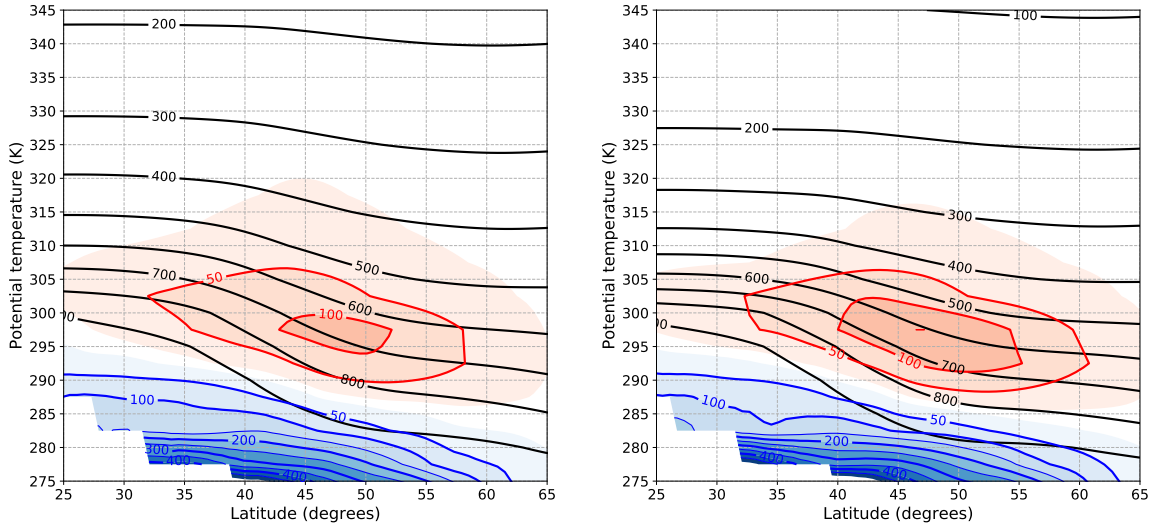

(a) $\Gamma_0 = 6.0$ K km^{-1} *(b)* $\Gamma_0 = 7.0$ K km^{-1}

Fig. 3.8: Zonal mean time mean total isentropic mass flux (red and blue contours) and zonal mean pressure (black contours) for different values of the temperature lapse rate. The zonal mean isentropic mass flux is plotted in kg m^{-1} K^{-1} s^{-1}. Red is northward flux, blue is southward flux. The shading starts at 10 kg m^{-1} K^{-1} s^{-1}. The zonal mean pressure is plotted in hPa. The time average is taken over model days 30 – 60. In these runs, $\alpha_N = 6.0 \cdot 10^{-6}$ s^{-1}, $y_{scale} = 500$ km, $U_0 = 50$ m s^{-2} and $k = 6$. The temperature lapse rate Γ_0 is different for both runs.

The model run shown in Figure 3.10b, is initialised with a straight zonal front without a superposed wave. Between 40° and 100°, the Newtonian cooling coefficient is $\alpha_N = 2.0 \cdot 10^{-6}$ s^{-1}. In the rest of the domain, the Newtonian cooling coefficient is equal to zero. The first development of growing baroclinic wave activity occurs after about 10 days. The growth is on the east side of the region where a non-zero Newtonian cooling coefficient is. The growth occurs thus in a region without any direct forcing. The next baroclinic life cycle grows again downstream of the previous one. The energy to grow baroclinic life cycles is thus advected eastward with the group speed of the Rossby waves, which is a higher speed than the phase speed of an individual wave. Between day 20 and 40, the strongest baroclinic life cycles grow and decay. The Rossby wave train that is formed in the domain has a wave number 6. This wave number is thus a wave number that is preferred by the system and the wave number with the largest growth rate.

3.6 Correlations between variables

The eddy MMF is the most important part of the total MMF in the baroclinic mass circulation. The eddy MMF seems to be driven by the eddy MPF. In Figure 3.11, the eddy MPF at 39.6°N and 307.5 K is plotted against the eddy MMF at 39.6°N and 307.5 K. Every point in the figure corresponds to a different model run, which is time averaged over a time period of 50 days, starting at day 12.5. A moderate positive correlation is found between these two variables around the centre of the jet. If the eddy MPF is almost equal to zero, the eddy MMF is very low. Higher eddy MPF at 39.6°N cause a higher MMF at 39.6°N. The relation between these variables is different than in the ERA-interim reanalysis, where a negative correlation is found (van Delden, 2018).

As seen in Figure 1.6, the eddy MPF fluxes can be up-gradient. To test the flux-gradient relation in the model solution, a time average (day 12.5 to 62.5) of the eddy MPF at 39.6°N and the average meridional gradient in absolute vorticity between 34.2°N and 45.0°N is given for all

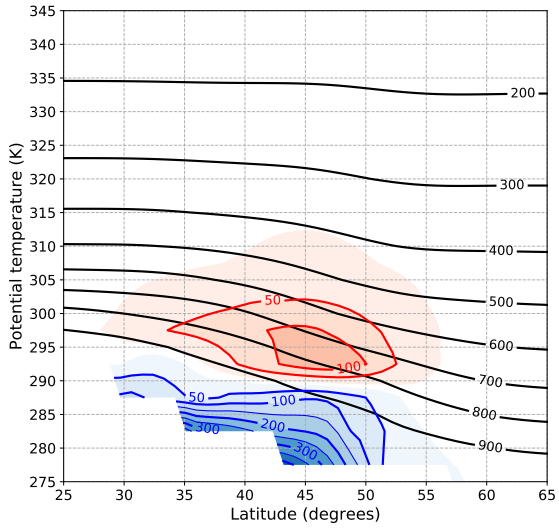

(a) $k = 5$, $y_{scale} = 400$ km, $U_0 = 50$ m s^{-1}

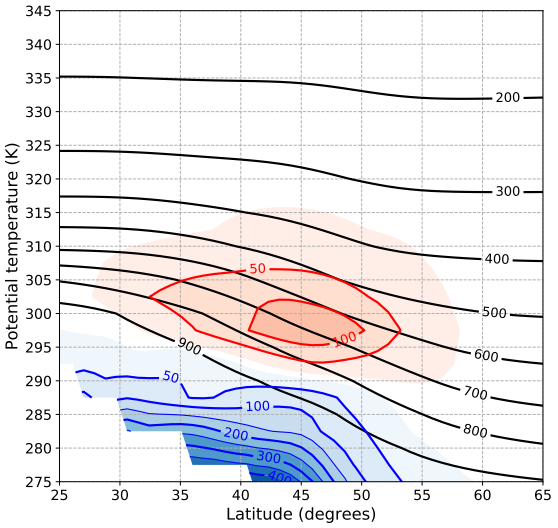

(b) $k = 5$, $y_{scale} = 600$ km, $U_0 = 50$ m s^{-1}

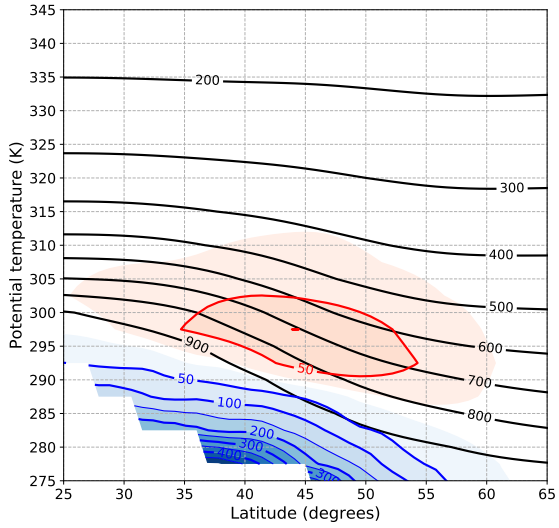

(c) $k = 6$, $y_{scale} = 600$ km, $U_0 = 41.67$ m s^{-1}

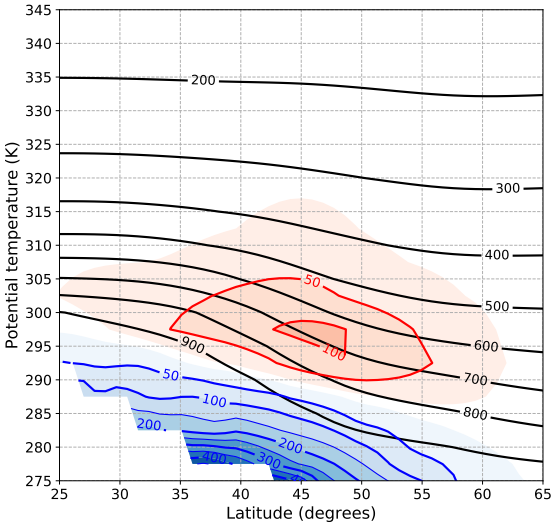

(d) $k = 6$, $y_{scale} = 400$ km, $U_0 = 62.5$ m s^{-1}

Fig. 3.9: Zonal mean time mean total isentropic mass flux (red and blue contours) and zonal mean pressure (black contours) for different initial wave numbers. The zonal mean isentropic mass flux is plotted in kg m^{-1} K^{-1} s^{-1}. Red is northward flux, blue is southward flux. The shading starts at 10 kg m^{-1} K^{-1} s^{-1}. The zonal mean pressure is plotted in hPa. The time average is taken over model days 30 – 60. In these runs, $\Gamma_0 = 6.5$ K km^{-1} and $\alpha_N = 1.0 \cdot 10^{-6}$ s^{-1}. The initial wave number k and the front parameters (y_{scale} and U_0) differ for the different runs.

model runs in Figure 3.12. These specific latitudes are taken to catch the northward branch of the MPF. The eddy MPF is taken in the centre of the latitudinal band for the absolute vorticity gradient. In all model runs, the eddy vorticity flux is positive (which means northward), whereas the gradient is positive (increasing in northward direction) as well. Furthermore, a higher absolute vorticity gradient is causing a higher eddy MPF. The model shows thus a similar pattern as seen in the ERA-interim reanalysis data.

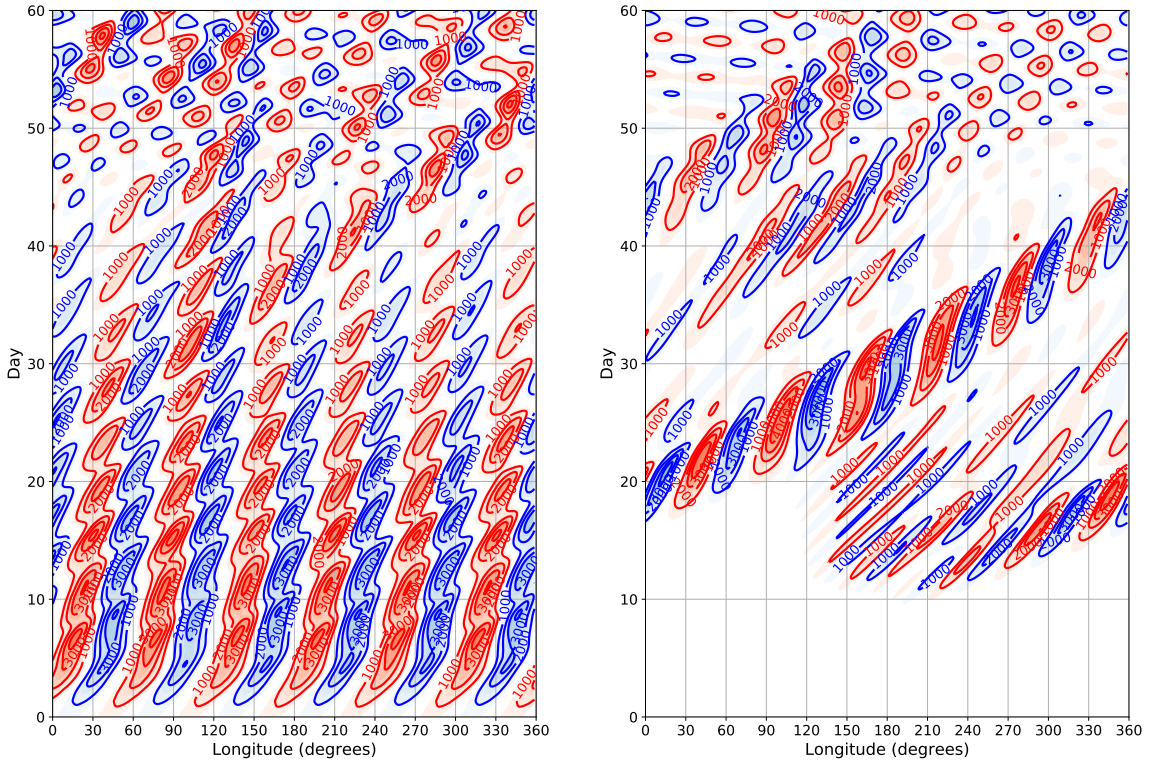

(a) $k = 6$ *(b)* $k = 0$

Fig. 3.10: Total meridional isentropic mass flux at 307.5 K and 45°N. The isentropic mass flux is given in kg m^{-1} K^{-1} s^{-1}. Red contours correspond to northward mass transport, blue contours to southward mass transport. The contour interval is 1000 kg m^{-1} K^{-1} s^{-1} and shading starts at 500 kg m^{-1} K^{-1} s^{-1}. In this runs, $\Gamma_0 = 6.5$ K km^{-1}, $y_{scale} = 500$ km and $U_0 = 50$ m s^{-2}. The Newtonian cooling coefficient is dependent on longitude and has the value $\alpha_N = 2.0 \cdot 10^{-6}$ s^{-1} between 40° and 100°. At all other longitudes, $\alpha_N = 0.5 \cdot 10^{-6}$ s^{-1} in Figure 3.10a and $\alpha_N = 0$ s^{-1} in Figure 3.10b. In Figure 3.10a, the intial wave number is $k = 6$. The solution of Figure 3.10b is initialised with a straight zonal front ($k = 0$).

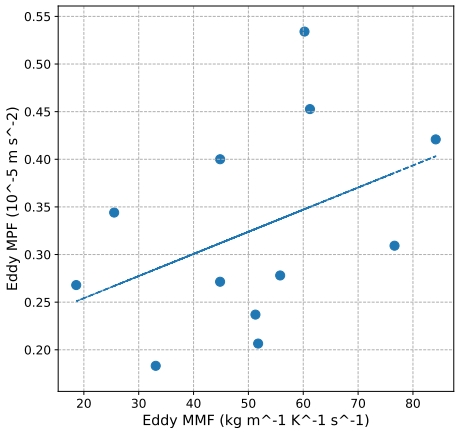

Fig. 3.11: The eddy MPF at 39.6°N and 307.5 K plotted against the eddy MMF at 45°N and 307.5 K. Every point is the time average of a different model run between day 12.5 and day 62.5. The positive correlation between both variables is moderate ($r = 0.42$).

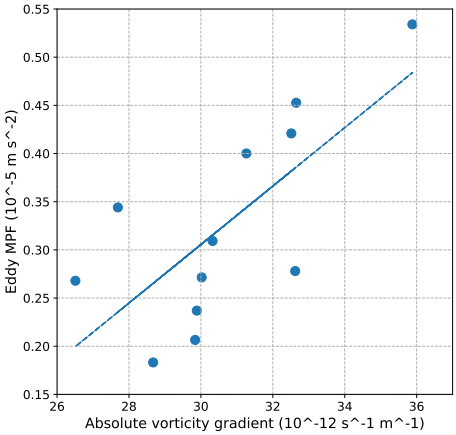

Fig. 3.12: The eddy MPF at 39.6°N and 307.5 K plotted against the average meridional gradient in absolute vorticity between 34.2°N and 45.0°N at 307.5 K. Every point is the time average of a different model run between day 12.5 and day 62.5. The positive correlation between both variables is strong ($r = 0.72$).

4. DISCUSSION

By comparing all results, the importance of the different parameters can be discussed. The initial wave number of the perturbation on the front is an important parameter. Different wave lengths give a different instability. The most preferred modes give large pulses of northward mass flux, whereas some wave numbers are not unstable at all and result in a small and constant mass flux caused by the fact that Newtonian cooling coefficient creates baroclinicity that needs to be 'removed' from the system.

The most important parameter that drives the northward MMF bulge at 45°N and 307.5 K is the Newtonian cooling coefficient. A doubling of this parameter almost leads to a doubling in MMF. A high Newtonian cooling creates a baroclinically unstable situation in a short time period. The baroclinicity has to be reduced by strong baroclinic life cycles that are associated with high MMF.

The static stability and front strength and width are also of some influence on the MMF, but this influence is much weaker than the influence of the Newtonian cooling coefficient.

4.1 Comparison to ERA-interim

The model results shown in Chapter 3 can be compared to reanalysis data from ERA-interim discussed in Section 1.5. As already seen in Section 3.1, the large scale features of the MMF in the model is similar to the MMF in reanalysis data. In the midlatitudes a northward branch of MMF is located around the 300 K isentrope. The order of magnitude of the maximum MMF in the model is comparable to the maximum MMF in the reanalysis data with values of about 100 kg s^{-1} m^{-1} K^{-1}.

As already shortly discussed in Section 3.1, the runs with a different initial wave number show different regimes. In reanalysis data, the different regimes are also visible. The model is a more idealistic situation than reality and maintains the translational symmetry. However, the solution with intial wave number $k = 5$ has some similarities with the positive NAM phase that occurred in the beginning of January 2007. Both contain relatively fast eastward propagating Rossby waves. The solution with intial wave number $k = 6$ shows similarities with the negative NAM phase. Both patterns are more stationary with preferred locations for northward MMF and preferred locations for southward MMF.

The MPF in the model (Figure 3.6) show also a similar pattern as in the reanalysis data (Figure 1.5). Around 40°N, the MPF is northward and at higher latitudes, the MPF is southward. In the low NAM regime, the northward MPF is more concentrated in the subtropics, where it reaches until 50°N, than in the positive NAM regime, where it reaches until 60°N. The MPF patterns in the solution have a northward MPF centred around 40°N and a southward MPF centred around 55°N. A large difference between a positive and negative NAM phase is not found in the model. However, the positive NAM phase is associated with stronger MPF than the negative phase. Wave number $k = 5$ leads to stronger MPF fluxes in the model and can therefore be associated with a more positive NAM phase. The southward shift in the jet is also larger in this solution. The magnitude of the MPF in the model solutions is lower than in the reanalysis data. This could be caused by the fact that the model simulates the tropospheric baroclinic life cycles, whereas the largest MPF signal in the reanalysis is visible in the lower stratosphere. The lower magnitude results furthermore in a smaller shift in the jet. The idealistic situation in the model forces the jet to the central latitude, which is a complete different setup compared to the real atmosphere.

4.2 Model restrictions

As we have seen, the model solutions result in realistic values for the MMF in the midlatitudes. The differences between the different model runs are however smaller than the difference that can be observed in the real atmosphere comparing different years. The 'positive NAM' and 'negative NAM' phases in the model are closer together than the positive NAM winters and the negative NAM winters in the reanalysis data. In reality the jet stream is more confined in a positive NAM phase. It can have two 'branches' in the negative NAM phase, one in the subpolar region and one in the subtropic region, which are jet streaks located at the troughs and ridges of the meandering Rossby wave. In the model, the jet is forced around 45°N and has no opportunity to meander strongly. The Newtonian cooling keeps the frontal zone at the central latitude, causing automatically a smaller spread in jet stream position. The forced location of the jet stream could explain the relatively small differences in total mass flux between the runs with a different initial wave number.

The model is a very idealistic display of reality. The boundary conditions are zonally symmetric and the initial conditions are already very baroclinically unstable in most runs. However, the run with a zonal front (see Section 3.5), shows that a complete zonal initial condition also results in baroclinic instability with a preferred wave number of $k = 6$.

The model furthermore only simulates the baroclinic zone. Any influences of the tropical Hadley circulation or the stratosphere are ignored. Even with this simplifications, the simulated MMF is comparable to the realistic values. A question that however cannot be answered is the influence of the Hadley circulation on the strength of the MMF. In reality, a part of the northward branch of the MMF originates from the Hadley circulation. The second part originates from the low level equatorward MMF caused by the baroclinic life cycles in cold air outbreaks. In the model, the Newtonian cooling forces the system back to the original state and delivers enough mass to the subtropical region for the circulation.

5. CONCLUSION

We have simulated the baroclinic life cycle with a 25 layer primitive equation model. In different model runs, the solution for various initial conditions and model parameters is calculated.

If the model has exactly similar boundary conditions, the solutions are still sensitive to different initial conditions. Certain initial wave numbers are preferred by the model. The fastest growing mode in our model is the mode with $k = 6$. This mode has development of baroclinic waves during the entire model period with corresponding peaks in the northward MMF at 45°N and 307.5 K. The model solution for $k = 6$ shows similarities with the negative phase in the NAM-index in reanalysis data. The modes $k = 4$ and $k = 5$ end as a 'wave train' with a doubling in wave number. The MMF is constant in time and the atmosphere seems to be marginally stable. These modes show patterns similar to the positive NAM-index phase seen in the reanalysis data.

An important parameter for the strength of the MMF is the Newtonian cooling coefficient α_N, the force that restores the initial baroclinically unstable situation. A high α_N results in high northward MMF at 45°N and 307.5 K. A more stable atmosphere, with a lower temperature lapse rate, decreases the MMF. Increasing the strength of the jet associated with the temperature front, the MMF is also increased.

All model results with constant model parameters result in translational symmetric solutions. Breaking the translational symmetry by prescribing a specific region with a higher Newtonian cooling coefficient, results in the development of baroclinic life cycles downstream of the region with high baroclinicity. A relatively narrow region with an enhanced baroclinic forcing is able to develop new life cycles downstream, even if a zonally symmetric condition is prescribed.

5.1 Outlook

The model is simplistic and further implementations can be done in the future. One of them is simulating a larger domain and prescribing with a seasonal cycle. On the large domain, the equilibrium temperature prescribed by James (1994) can be used. In Appendix A, some calculation are given for the inclusion of the seasonal cycle in the model using the equilibrium temperature distribution by James (1994).

A further interesting test for the model, would be to include a Hadley circulation. With this implementation, the flow of mass around 30°N can be simulated. A part of the downwelling at the northern end of the Hadley circulation flows northward to the poles and a part flows back to the equator. In isentropic coordinates, these northward and southward flows are at the same height (see Figure 1.3). By simulation the life cycle, one can investigate the amount of mass that is pumped in the midlatitude circulation by the Hadley circulation.

Another addition to the model is a more realistic radiation model. The radiation part is now parametrised very simple by a constant Newtonian cooling coefficient. With a more realistic radiation model the diabatic processes can be studied in more detail.

The addition of orography in the model is a fourth implementation that can give more insight in the processes that play a role in reality in the formation and location of baroclinic waves.

Appendix A

SUGGESTED ADDITIONS TO THE MODEL

In this Appendix, an initial geopotential for the PeN-model is derived using the potential temperature given by James (1994). The potential temperature as a function of latitude is given by Eq. (4.16) in James:

$$\theta = \theta_0 + \frac{\Delta\theta_{NS}}{2}\sin\phi + \Delta\theta_{EP}\left(3\sin^2\phi - 1\right) \tag{A.1}$$

where $\Delta\theta_{NS}$ is the difference in temperature between the North and South Pole. The temperature difference can be varied to include the seasonal cycle in the model. More about the varying $\Delta\theta_{NS}$ can be found in Section A.3. $\Delta\theta_{EP}$ represents the equator to pole temperature difference, which is by James (1994) set at 40 K. θ_0 is the global average radiative equilibrium temperature, which is set at 255 K in James (1994). In our model, $\theta_0 = \theta_0(z)$ to get the height dependence in the model, given by (van Delden, 2017)

$$\theta_0(z) = \theta_0(0) - \Gamma_0\left(\frac{p_0}{p}\right)^{\kappa} z \tag{A.2}$$

where Γ can be tuned, but is standard set to 6.5 K/km.

A.1 β-plane model

Firstly, we can calculate the meridional gradient of the temperature distribution

$$\frac{\partial T}{\partial y} = \frac{1}{a}\left(\frac{p}{p_0}\right)^{\kappa}\frac{\partial\theta}{\partial\phi} = \frac{1}{a}\left(\frac{p}{p_0}\right)^{\kappa}\left(\frac{\Delta\theta_{NS}}{2}\cos\phi + 6\Delta\theta_{EP}\sin\phi\cos\phi\right) \tag{A.3}$$

The thermal wind balance reads

$$\frac{\partial u_g}{\partial p} = \frac{R}{pf_0}\frac{\partial T}{\partial y} \tag{A.4}$$

By integrating Equation A.4 over p, we obtain the geostrophic flow

$$u_g = \left[\left(\frac{p}{p_0}\right)^{\kappa} - 1\right]\frac{c_p}{af_0}\left(\frac{\Delta\theta_{NS}}{2}\cos\phi + 6\Delta\theta_{EP}\sin\phi\cos\phi\right) \tag{A.5}$$

where f_0 is the Coriolis parameter at 45°N. In Figure A.1, the geostrophic wind profile according to Equation A.5 is plotted for the northern hemisphere. This formula gives one jet in the northern hemisphere, with a wind maximum at 45°N at the top of the atmosphere with a strength of about 200 m/s, which is very strong.

By using the geostrophic wind and the relation $-f_0 u_g = \partial\Phi/\partial y$, we can calculate the geopotential

$$\Phi = \Phi_0 + c_p\left[1 - \left(\frac{p}{p_0}\right)^{\kappa}\right]\left(\frac{\Delta\theta_{NS}}{2}\sin\phi + 3\Delta\theta_{EP}\sin^2\phi\right) \tag{A.6}$$

This geopotential has also a large variation over the northern hemisphere. At 900 hPa, $\Phi(0°) - \Phi(90°) = 17\cdot 10^3$ m^2 s^{-2}, whereas this difference in the example in Section 10.7 of van Delden (2017) is $8\cdot 10^2$ m^2 s^{-2}.

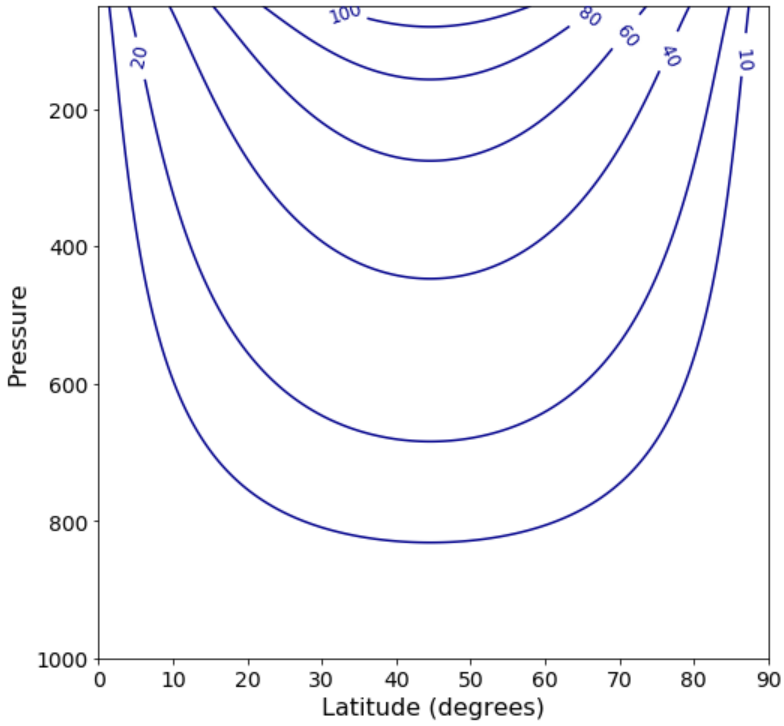

Fig. A.1: The geostrophic wind distribution on the northern hemisphere according to Equation A.5. The values used for this plot are $p_0 = 1000$ hPa, $\Delta\theta_{NS} = -10$ K (situation in January) and $\Delta\theta_{EP} = -40$ K. The highest level plotted is at 50 hPa.

A.2 Reducing temperature gradient at height

Because the geopotential from Equation A.6 gives too high geostrophic wind speeds in the jet, we need to reconsider the chosen initial condition. The starting point is still the given temperature gradient by James (Equation A.1). However, now we will reduce the temperature gradient at height. The height dependence of this reduction is introduced as

$$\frac{\partial\theta_0}{\partial\phi} = \frac{\Delta\theta_{TOA}}{\pi/2}\left(1+\cos\left(\frac{\pi p}{p_0}\right)\right) \tag{A.7}$$

with $\Delta\theta_{TOA}$ the reduction in temperature gradient at the top of the atmosphere.

By choosing the latitude-dependent terms in the temperature height independent, we obtain a new temperature distribution

$$\begin{aligned}\theta(\phi,p) = \theta_0(0)\left[1+\frac{\Gamma_0 R}{g}\ln\left(\frac{p}{p_0}\right)\right]\left(\frac{p_0}{p}\right)^{\kappa} + \frac{50\phi}{\pi/2}\left[1+\cos\left(\frac{\pi p}{p_0}\right)\right] \\ +\frac{\Delta\theta_{NS}}{2}\sin\phi + \Delta\theta_{EP}\left(3\sin^2\phi - 1\right)\end{aligned} \tag{A.8}$$

With the new temperature distribution, we obtain a new geostrophic wind relation, given by

$$\begin{aligned}u_g(\phi,p) = \frac{2R\Delta\theta_{TOA}}{af_0\pi}\left[\mathrm{Ci}\left(\frac{\pi p}{p_0}\right) - \mathrm{Ci}\left(\pi\right) + \ln\left(\frac{p}{p_0}\right)\right] \\ +\frac{R}{2af_0}\left[\Delta\theta_{NS}\cos\phi + 6\Delta\theta_{EP}\sin 2\phi\right]\ln\left(\frac{p}{p_0}\right)\end{aligned} \tag{A.9}$$

where $\mathrm{Ci}(x)$ is the cosine integral function. The corresponding geostrophic wind profile is plotted in Figure A.2. The maximum of the geostrophic wind is now significantly lower than in Figure A.1.

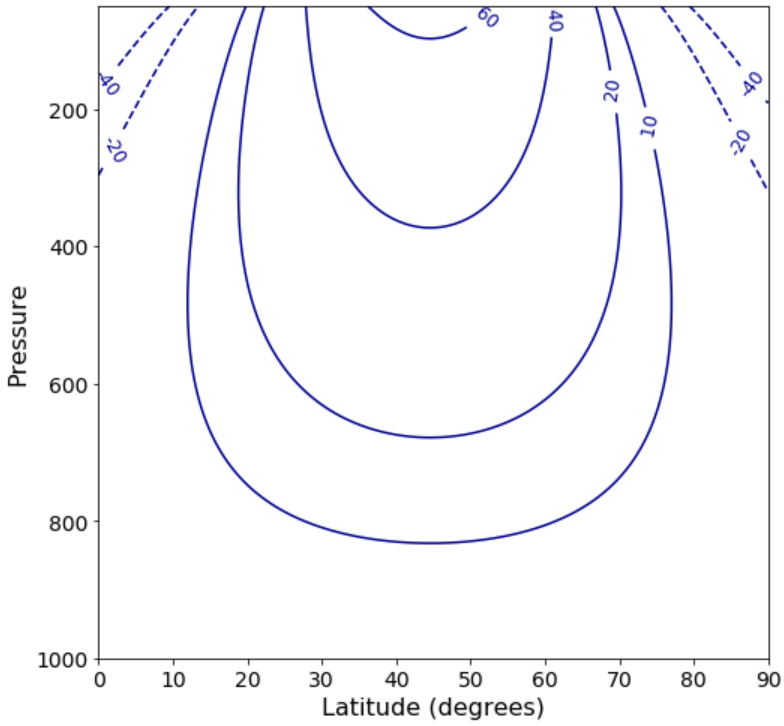

Fig. A.2: The geostrophic wind distribution (in m/s) on the northern hemisphere according to Equation A.9. The values used for this plot are $p_0 = 1000$ hPa, $\Delta\theta_{NS} = -10$ K (situation in January), $\Delta\theta_{EP} = -40$ K and $\Delta\theta_{TOA} = 80$ K. The highest level plotted is at 50 hPa.

A disadvantage of the new equation is that we obtain high easterly winds at high altitude above the poles and the equator.

The geopotential corresponding to the sketched situation is given by

$$\Phi(\phi,p) = -RT_0 \ln\left(\frac{p}{p_0}\right) - \frac{2R\phi\Delta\theta_{TOA}}{\pi}\left[\mathrm{Ci}\left(\frac{\pi p}{p_0}\right) - \mathrm{Ci}\left(\pi\right) + \ln\left(\frac{p}{p_0}\right)\right] + \frac{R}{2}\left[\Delta\theta_{NS}\sin\phi + 3\Delta\theta_{EP}\cos 2\phi\right]\ln\left(\frac{p}{p_0}\right) \tag{A.10}$$

The geopotential height ($Z = \Phi/g$) is plotted in Figure A.3.

A.2.1 Extra addition

The geostrophic wind had large negative values at height above the poles and equator. By adding an extra factor to the meridional gradient of θ_0, we can prevent this. The gradient of θ_0 now becomes

$$\frac{\partial\theta_0}{\partial\phi} = \frac{\Delta\theta_{TOA}}{\pi/2}\left(1 + \cos\left(\frac{\pi p}{p_0}\right)\right)\left(1 - \cos 4\phi\right) \tag{A.11}$$

By calculating the geostrophic wind, we obtain the following relation

$$u_g(\phi,p) = \frac{\Delta\theta_{TOA}R}{af_0\pi}\left[\left(\cos 4\phi - 1\right)\left(\mathrm{Ci}(\pi) + \ln(p_0)\right) + 2\sin^2 2\phi\left(\mathrm{Ci}\left(\frac{p\pi}{p_0}\right) + \ln(p)\right)\right] + \frac{R}{2af_0}\left(\Delta\theta_{NS}\cos\phi + 6\Delta\theta_{EP}\sin 2\phi\right)\ln\left(\frac{p}{p_0}\right) \tag{A.12}$$

which is shown in Figure A.4.

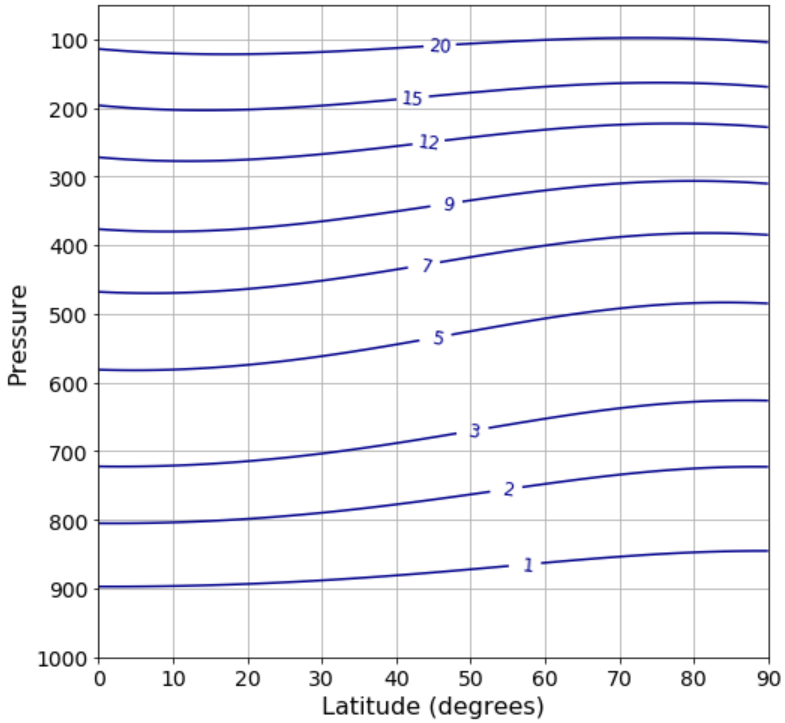

Fig. A.3: The geopotential height in km on the northern hemisphere according to Equation A.10. The values used for this plot are $p_0 = 1000$ hPa, $T_0 = 255$ K, $\Delta\theta_{NS} = -10$ K (situation in January), $\Delta\theta_{EP} = -40$ K and $\Delta\theta_{TOA} = 80$ K.

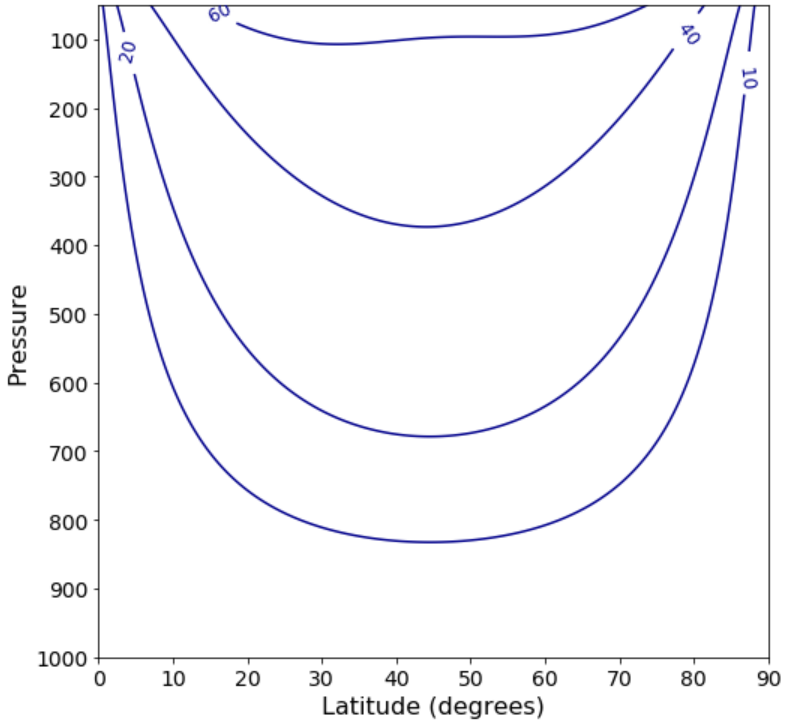

Fig. A.4: The geostrophic wind distribution (in m/s) on the northern hemisphere according to Equation A.12. The values used for this plot are $p_0 = 1000$ hPa, $\Delta\theta_{NS} = -10$ K (situation in January), $\Delta\theta_{EP} = -40$ K and $\Delta\theta_{TOA} = 80$ K. The highest level plotted is at 50 hPa.

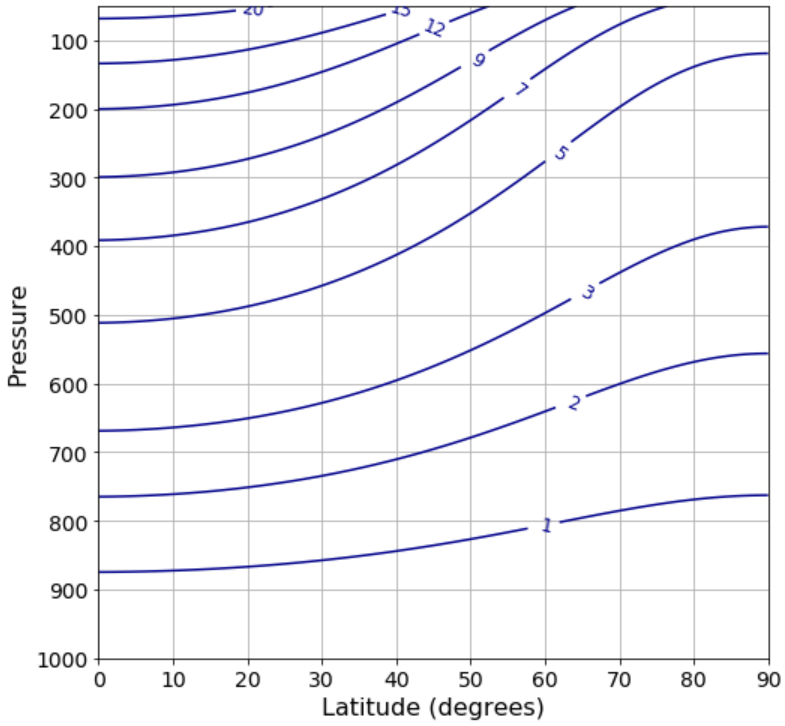

Fig. A.5: The geopotential height in km on the northern hemisphere according to Equation A.13. The values used for this plot are $p_0 = 1000$ hPa, $T_0 = 255$ K, $\Delta\theta_{NS} = -10$ K (situation in January), $\Delta\theta_{EP} = -40$ K and $\Delta\theta_{TOA} = 80$ K.

The corresponding geopotential is given by

$$\begin{aligned}\Phi(\phi, p) = &-RT_0 \ln\left(\frac{p}{p_0}\right) - \frac{R}{2}\left[\Delta\theta_{NS}\sin\phi + 6\Delta\theta_{EP}\sin^2\phi\right]\ln\left(\frac{p}{p_0}\right) \\ &-\frac{R\Delta\theta_{TOA}}{4\pi}\left[\mathrm{Ci}\left(\frac{\pi p}{p_0}\right) - \mathrm{Ci}\left(\pi\right) + \ln\left(\frac{p}{p_0}\right)\right](\sin 4\phi - 4\phi)\end{aligned} \tag{A.13}$$

which is ploted in Figure A.5

A.3 The seasonal cycle in the model

In this section, we try to obtain a first guess for the seasonal cycle by finding a function for $\Delta\theta_{NS}$. For this the winter and summer temperatures for both poles are estimated at -40°C and 0°C, respectively, for the north pole and -60°C and -30°C, respectively, for the south pole[1].

We assume that the lowest temperature at the north pole and the highest temperature at the south pole is reached at 15 January (day 15). By furthermore assuming a sinusoidal profile for the temperature difference, $\Delta\theta_{NS}$ is given by

$$\Delta\theta_{NS}(t) = 25 - 35\cos\left(\frac{2\pi}{365}(t - 15)\right) \tag{A.14}$$

with t the day of the year.

This equation is a first draft for the seasonal cycle. A plot of the corresponding radiative equilibrium temperature is shown in Figure A.6. A more advanced equation can be used by e.g. using reanalysis data of an averaged surface air temperature above 80°N and 80°S throughout the year.

[1] `http://polardiscovery.whoi.edu/poles/weather.html`

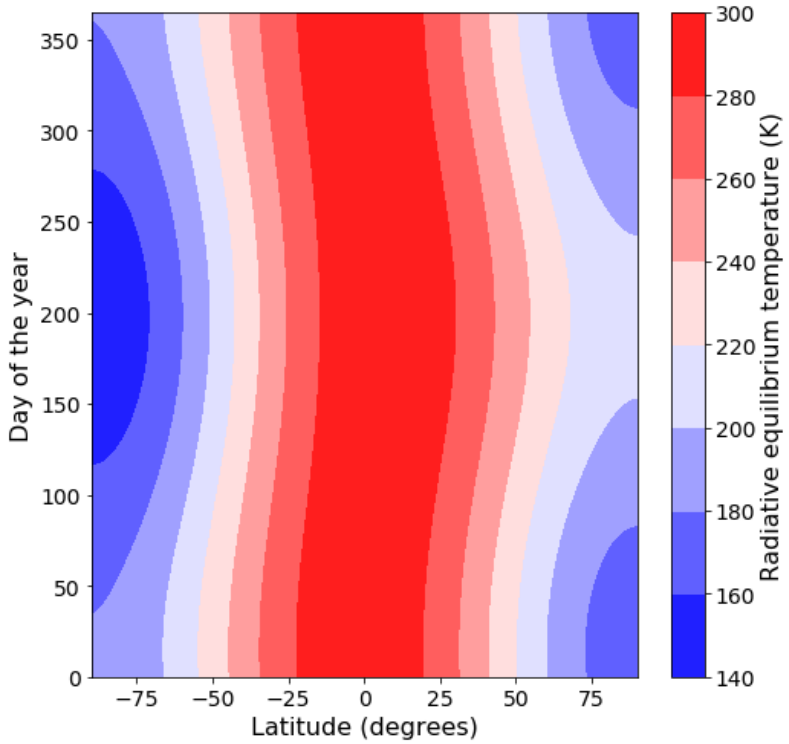

Fig. A.6: The radiative equilibrium temperature θ_e at the surface, using $\theta_0 = 255$ K, $\Delta\theta_{EP} = -40$ K and Equation A.14, plotted for all latitudes and a year of time.

BIBLIOGRAPHY

M.H.P. Ambaum and L. Novak. A nonlinear oscillator describing storm track variability. *Quarterly Journal of the Royal Meteorological Society*, 140(685):2680–2684, 2014.

M.H.P. Ambaum, B.J. Hoskins, and D.B. Stephenson. Arctic oscillation or north atlantic oscillation? *Journal of Climate*, 14(16):3495–3507, 2001.

M.L. Blackmon. A climatological spectral study of the 500 mb geopotential height of the northern hemisphere. *Journal of the Atmospheric Sciences*, 33(8):1607–1623, 1976.

E.K.M. Chang and I. Orlanski. On the dynamics of a storm track. *Journal of the atmospheric sciences*, 50(7):999–1015, 1993.

J.G. Charney. The dynamics of long waves in a baroclinic westerly current. *Journal of Meteorology*, 4(5):136–162, 1947.

D.P. Dee, S.M. Uppala, A.J. Simmons, P. Berrisford, P. Poli, S. Kobayashi, U. Andrae, M.A. Balmaseda, G. Balsamo, P. Bauer, et al. The era-interim reanalysis: Configuration and performance of the data assimilation system. *Quarterly Journal of the royal meteorological society*, 137(656): 553–597, 2011.

W. Ferrel. The motion of fluids and soilds. *Math. Monthly*, 1:140–147,210–216,300–307,366–372, 1859.

G. Hadley. Concerning the cause of the general trade-winds: By geo. hadley, esq; f. r. s. *Philosophical Transactions (1683-1775)*, 39:58–62, 1735. ISSN 02607085.

I.M. Held and A.Y. Hou. Nonlinear axially symmetric circulations in a nearly inviscid atmosphere. *Journal of the Atmospheric Sciences*, 37(3):515–533, 1980.

J.R. Holton and G.J. Hakim. *An introduction to dynamic meteorology*, volume 88. Academic press, 2012.

B.J. Hoskins and P.J. Valdes. On the existence of storm-tracks. *Journal of the atmospheric sciences*, 47(15):1854–1864, 1990.

I.N. James. *Introduction to circulating atmospheres*. Cambridge University Press, 1994.

H.-L. Kuo. Three-dimensional disturbances in a baroclinic zonal current. *Journal of Meteorology*, 9(4):260–278, 1952.

N.-C. Lau and J.M. Wallace. On the distribution of horizontal transports by transient eddies in the northern hemisphere wintertime circulation. *Journal of the Atmospheric Sciences*, 36(10): 1844–1861, 1979.

J. Li and J.X.L. Wang. A modified zonal index and its physical sense. *Geophysical Research Letters*, 30(12), 2003.

R.S. Lindzen and B. Farrell. A simple approximate result for the maximum growth rate of baroclinic instabilities. *Journal of the atmospheric sciences*, 37(7):1648–1654, 1980.

E.N. Lorenz. Seasonal and irregular variations of the northern hemisphere sea-level pressure profile. *Journal of Meteorology*, 8(1):52–59, 1951.

E.N. Lorenz. *The nature and theory of the general circulation of the atmosphere*, volume 218. World Meteorological Organization Geneva, 1967.

L.R. Mendez-Nunez and J.J. Carroll. Comparison of leapfrog, smolarkiewicz, and maccormack schemes applied to nonlinear equations. *Monthly weather review*, 121(2):565–578, 1993.

L. Novak, M.H.P. Ambaum, and R. Tailleux. The life cycle of the north atlantic storm track. *Journal of the Atmospheric Sciences*, 72(2):821–833, 2015.

L. Novak, M.H.P. Ambaum, and R. Tailleux. Marginal stability and predator–prey behaviour within storm tracks. *Quarterly Journal of the Royal Meteorological Society*, 143(704):1421–1433, 2017.

N.A. Phillips. Energy transformations and meridional circulations associated with simple baroclinic waves in a two-level, quasi-geostrophic model. *Tellus*, 6(3):274–286, 1954.

N.A. Phillips. The general circulation of the atmosphere: A numerical experiment. *Quarterly Journal of the Royal Meteorological Society*, 82(352):123–164, 1956.

C.-G. Rossby. Relation between variations in the intensity of the zonal circulation of the atmosphere and the displacements of the semi-permanent centers of action. *J. Marine Res.*, 2:38–55, 1939.

T. Schneider. The general circulation of the atmosphere. *Annu. Rev. Earth Planet. Sci.*, 34: 655–688, 2006.

A.J. Simmons and B.J. Hoskins. The life cycles of some nonlinear baroclinic waves. *Journal of the Atmospheric Sciences*, 35(3):414–432, 1978.

V. Starr. *Physics of negative viscosity phenomena*. McGraw-Hill, 1968.

D.W.J. Thompson and J.M. Wallace. The arctic oscillation signature in the wintertime geopotential height and temperature fields. *Geophysical research letters*, 25(9):1297–1300, 1998.

D.W.J. Thompson and J.M. Wallace. Annular modes in the extratropical circulation. part i: Month-to-month variability. *Journal of climate*, 13(5):1000–1016, 2000.

J. Thomson. Bakerian lecture.—on the grand currents of atmospheric circulation. *Proceedings of the Royal Society of London*, 51(308-314):42–46, 1892.

C.D. Thorncroft, B.J. Hoskins, and M.E. McIntyre. Two paradigms of baroclinic-wave life-cycle behaviour. *Quarterly Journal of the Royal Meteorological Society*, 119(509):17–55, 1993.

A.J. van Delden. *The General Circulation of the Atmosphere*. Department of Physics, Utrecht University, 2017.

A.J. van Delden. Physics of the "northern annular mode" at sea level, 2018.

G.T. Walker. Correlations in seasonal variations of weather. i. a further study of world weather. *Mem. Indian Meteorol. Dep.*, 24:275–332, 1924.

J.M. Wallace. North atlantic oscillatiodannular mode: two paradigms—one phenomenon. *Quarterly Journal of the Royal Meteorological Society*, 126(564):791–805, 2000.

J.M. Wallace and D.S. Gutzler. Teleconnections in the geopotential height field during the northern hemisphere winter. *Monthly Weather Review*, 109(4):784–812, 1981.